QUADRUPOLE INTERACTIONS OF Ta^{181} IN HfO_2

QUADRUPOLE INTERACTIONS OF Ta^{181} IN A POLYCRYSTALLINE HAFNIUM DIOXIDE ENVIRONMENT.

BY

PHILIP REGINALD GARDNER, B.Sc.

A Thesis

Submitted to the School of Graduate Studies

in Partial Fulfilment of the Requirements

for the Degree

Master of Science

McMaster University

(December) 1969

MASTER OF SCIENCE (1969) McMASTER UNIVERSITY

(Physics) Hamilton, Onatrio

TITLE: Quadrupole Interactions of Ta^{181} in a Polycrystalline HfO_2 Environment.

AUTHOR: Philip Reginald Gardner, B.Sc. (University of Sussex).

SUPERVISOR: Dr. W. V. Prestwich

NUMBER OF PAGES: 108

SCOPE AND CONTENTS:

A study of the quadrupole interactions of Ta^{181} in a polycrystalline hafnium dioxide environment is described in this work. A general introduction to the concepts of angular correlations in nuclear physics is given in Chapter 1 followed by the main outlines of the theory of quadrupole interactions. Instrumental effects involved in the measurement of such an interaction and the analysis of data using Fourier transform methods are discussed. Descriptions of the structure of HfO_2, the factors involved in attaining short time resolutions in timing and the experimental system and methods used in the study are given. The final two chapters contain the results and conclusions with comparison with results from other works.

ACKNOWLEDGEMENTS

In expressing my acknowledgements I realise that on joining Dr. Prestwich's group and undertaking this study I was almost completely ignorant of all the factors involved in the art of experimental nuclear physics and that the modest amount of knowledge and skills attained to date are largely due to his expert guidance and instruction. Many of the ideas expressed in this work originated from his inspiration. Due regard must also be made of the advice and assistance willingly offered by James Boulter and Dr. Ben Arad. Credit for the diagrams goes to my artistic wife Vanessa. Mrs. Prestwich kindly undertook the task of typing the manuscript.

TABLE OF CONTENTS

LIST OF ILLUSTRATIONS

LIST OF TABLES

CHAPTER I

INTRODUCTION

The angular distribution $W(\theta)$ of radiation emitted by radioactive nuclei is defined in terms of the probability $dW = W(\theta)d\Omega$ for the emission of radiation into a solid angle $d\Omega$ where θ is the angle between the direction of the radiation and some fixed direction. The radiations can be electromagnetic gamma radiation or particles such as electrons, positrons, alpha particles or mesons etc. However, in this work we shall be confined to the study of the angular distributions of gamma radiations.

The angular distribution of gamma radiation $W(\theta)$ from a particular nucleus in free space is analagous to that of electromagnetic radiation emitted from an oscillating dipole which gives the familiar radiation pattern shown in Figure 1.1 with the form:

$$W(\theta) = \text{constant} \times \sin^2(\theta)$$

In the case of nuclear radiations the form of $W(\theta)$ is strongly dependent on the nuclear properties such

as the spins of the nuclear levels and on the multipolarity of the emitted radiation, so such distributions have been widely studied to determine nuclear properties. The angular distribution of radiations emitted from a nucleus experiencing the influence of extra-nuclear electric or magnetic fields will be altered with respect to that of a nucleus in free space and one obtains a "perturbed" distribution. Since most nuclei are studied in condensed matter they will always be experiencing the fields and field gradients present in the inter-nuclear space due to the surrounding atoms and molecules, and so studies of such effects provide a link between solid state and nuclear physics by providing a means to investigate the properties of the environments of nuclei in solids or liquids using fairly well understood nuclear properties.

In order that an assembly of radiating nuclei in matter may give an overall anisotropic distribution of radiation many of them would obviously have to possess the same orientation with respect to a particular direction. This orientation can be obtained in several ways:

1. By cooling the source while under the influence of electric or magnetic fields to very low temperatures, when the Boltzmann distribution will insure a net alignment of the nuclear spins.

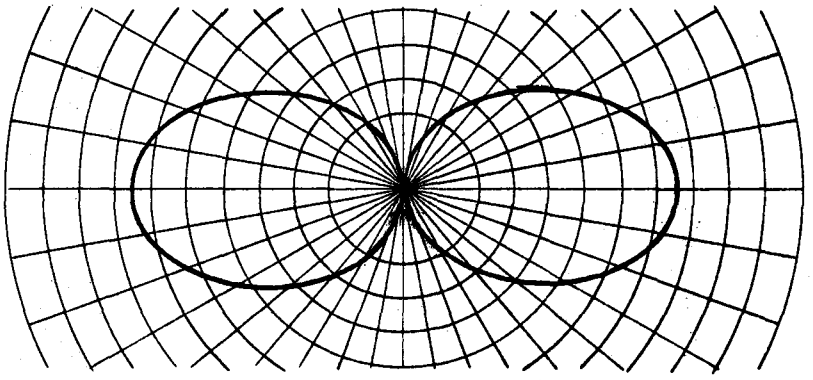

FIGURE 1·1 Dipole radiation pattern.

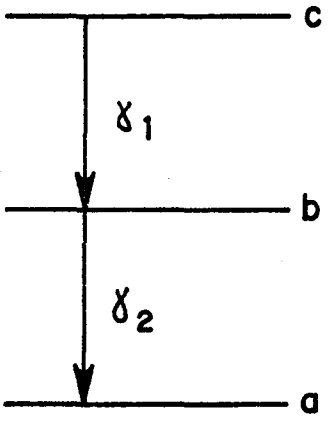

FIGURE 1·2 A decay scheme for excited nuclear states.

2. By involving certain nuclear reactions in which orientated reaction products are produced. For instance, if a polarised particle is absorbed into a nucleus, or an unpolarised particle is absorbed or scattered through a channel involving non-vanishing angular momentum, a net orientation will result.

3. By the selection of nuclei with aligned spins. Consider a decay scheme of the type shown in Figure 1.2 involving the decay of two excited states b and c of a nucleus to the ground state via two successive gamma radiations γ_1 and γ_2. Choosing only those nuclei which emit the first radiation γ_1 into a given direction is equivalent to selecting nuclei with partially aligned spins. The angular distribution of the second radiation γ_2 will then be that of an assembly of radiating nuclei with their spins pointing preferentially in a certain direction. This angular distribution is dependent on the properties of the radiative cascade and is called the "angular correlation of successive radiations" and is the mechanism to be referred to henceforth in this work. Angular correlations can exist for cascades involving Beta and Alpha decays as well, but it is those of successive gamma radiations that will concern us.

For an angular correlation to be unperturbed it can be appreciated that the orientation of the nucleus

must remain unchanged between the times of emission of γ_1 and γ_2 in the above example, i.e., during the lifetime of the intermediate state b in Figure 1.2. If the nuclear electric or magnetic moments interact with fields or field gradients present in the surroundings the nuclear moments will precess about the direction of the field like a gyroscope precessing in a gravitational field; thus introducing a periodic change in the nuclear orientation. If the lifetime of the intermediate state is significant compared to the precession period the angular correlation between γ_1 and γ_2 will be perturbed. The study of such "perturbed angular correlations" (PAC) yields information on the fields present in the nuclear surroundings.

One can gain similar information by using nuclear or paramagnetic resonance techniques but the PAC methods have several advantages:

1. No external radio-frequency fields have to be applied in PAC methods. In the case of quadrupole moments interacting with the electric field gradients in crystal structures (which is what we are interested in) the transitions between the hyperfine splittings produced by the interaction may be induced by an applied r.f. field, but the transition probabilities are low. This results in a low sensitivity for resonance methods,

which is reflected in the fact that it is possible to make a PAC measurement with about 10^8 active atoms while resonance methods require up to 10^{17} atoms. This is a particular advantage when applied to the study of impurities in semiconductors.

2. PAC methods allow the possibility of studying the quadrupole interactions of short lived nuclear levels.

3. Metal crystals can be studied by PAC methods without the difficulties arising from the skin effects that occur with resonance methods.

4. Resonance methods can only be applied to nuclei in their ground state and as a nucleus must have a spin of more than 1/2 in order to possess a quadrupole moment, resonance techniques cannot be applied to study quadrupole interactions in nuclei with a ground state spin of 1/2. However, if there is a suitable excited state with a higher spin, PAC methods may be used. The reverse of the above is, of course, also true and sometimes no cascade suitable for a PAC measurement exists among the isotopes of a nucleus, but its ground state spin may make quadrupole studies with resonance methods possible.

However, PAC methods do suffer from the following disadvantages when compared to resonance ones:

1. Resonance techniques tend to achieve a higher accuracy and a broader range of application.

2. With PAC methods the nuclear environment is often in an excited state following irradiation or beta decay to the gamma cascade being studied. This can introduce unknown effects while resonance methods study the environment in its ground state.

We now turn to a brief description of the basic experimental methods employed in the study of angular correlations of successive nuclear radiations. A detailed description of the techniques used in this work will be found in Chapter 7. The basic arrangement is shown in Figure 1.3 and consists of two detectors 1 and 2 subtending an angle θ at the source. These detectors respond to all radiations falling in their solid angles from a nuclear decay such as that in the scheme shown in Figure 1.2, but the coincidence analyzer will only select pairs of pulses from the detectors corresponding to γ_1 being detected in detector 1, and γ_2 in detector 2, if these two pulses arrive within a time τ_R, the resolving time of the coincidence circuit. Such a system ensures that γ_1 and γ_2 in each pair of pulses passed by the coincidence circuit come from the same nucleus. Chance coincidences arising from pairs of pulses from gamma radiations with members originating from different nuclei will, of course, also occur but may be minimized by the proper choice of τ_R and the source strength.

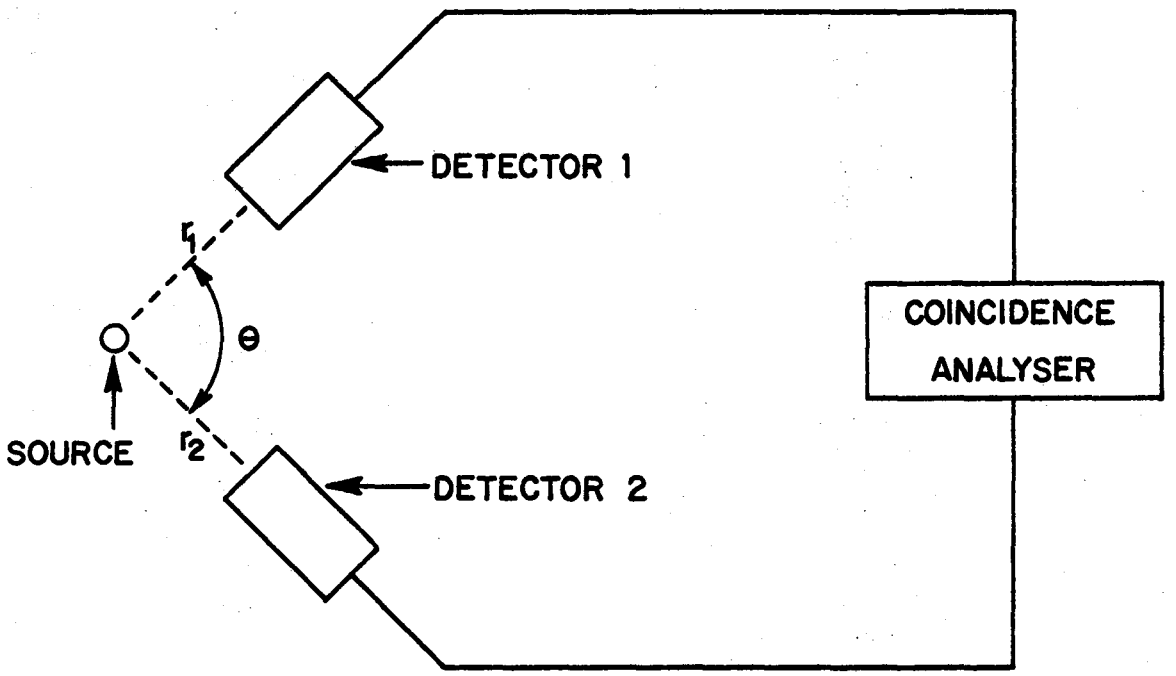

FIGURE 1·3 Schematic diagram of the experimental arrangement used for the measurement of an angular correlation.

$W(\theta)$ is then expressed as the number of coincidences per unit time as a function of angle θ. The distribution of time differences between the emissions of γ_1 and γ_2 will be the exponential decay of the intermediate level with a lifetime τ_N. If τ_N is not insignificant compared to the time period of any effects due to interactions of the nuclear moments with extra-nuclear fields the angular correlation will be perturbed.

CHAPTER 2

THE THEORY OF THE PERTURBATION OF ANGULAR CORRELATIONS BY STATIC QUADRUPOLE INTERACTIONS

The unperturbed angular correlation function $W(\theta)$ for successive nuclear radiations can be shown[1] to have the form:

$$W(\theta) = \sum_k A_{k_1 k_2} P_k(\cos\theta) \qquad 2.1$$

where the $P_k(\cos\theta)$ are Legendre Polynomials and the $A_{k_1 k_2}$ can be written, with k taking even values only as:

$$A_{k_1 k_2} = f_{1k} f_{2k} \qquad 2.2$$

f_{1k} being a factor depending only on the properties of the first transition, say from level c to level b in Figure 1.2, and similarly f_{2k} depends only on the properties of the transition from level b to level a.

The effect of the influence of an extranuclear field on the above is a change in nuclear orientation with time, which can be described by an additional

factor in equation 2.1, giving:

$$W(\theta,t) = \sum_{k} A_{k_1 k_2} G_{k_1 k_2}(t) P_k(\cos\theta) \qquad 2.3$$

$G(t)$, is called the "attenuation factor". If the finite time resolution τ of the coincidence circuits used in the measuring system is much less than τ_n, the lifetime of the intermediate state, $G(t)$, is called the "differential" attenuation factor. If $\tau >> \tau_n$ then the "integral" attenuation factor is measured. In this work we are concerned with "static", i.e., non time dependant, interactions as opposed to time dependant ones which may arise in liquids through relaxation phenomena. These static interactions involve, in our case, quadrupole moments and the electric field gradients existing in crystal lattices.

2.1 THE THEORY OF STATIC ELECTRIC QUADRUPOLE INTERACTIONS

The theory of quadrupole interactions have been treated by many authors[2,3,4,5,6,7], and only a brief resumé will be given here. The Hamiltonian describing the interaction can be written as:

$$K_Q = \frac{4\pi}{5} \sum_{q} (-)^q T_q^{(2)} V_{-q}^{(2)} \qquad 2.4$$

$T^{(2)}$ being a second rank tensor of the nuclear quadrupole

moment with the components:

$$T_q^{(2)} = \sum_p e_p r_p^2 Y_2^q(\theta_p,\phi_p) \qquad 2.5$$

The e_p are point charges in the nucleus at the points (r_p,θ_p,ϕ_p) and $V^{(2)}$ is the tensor operator of the classical external field gradient with spherical components:

$$V_q^{(2)} = \sum_c (e_c/r_c^3) Y_2^q(\theta_c,\phi_c) \qquad 2.6$$

Here the e_c are the point charges in the crystal lattice at the points (r_c,θ_c,ϕ_c). In terms of arbitary cartesian coordinates (x'y'z') and corresponding electric field gradients $V_{x'x'} = \frac{d^2V}{dx'^2}$, $V_{x'y'}$, $V_{y'y'}$, etc.:

$$V_0^{(2)} = \tfrac{1}{4}(5/\pi)^{1/2} V_{z'z'}$$

$$V_{\pm}^{(2)} = \tfrac{-1}{+2}(5/6\pi)^{1/2}(V_{x'z'} \pm iV_{y'z'}) \qquad 2.7$$

$$V_{\pm 2}^{(2)} = \tfrac{1}{4}(5/6\pi)^{1/2}(V_{x'x'}-V_{y'y'} \pm 2iV_{x'y'})$$

One can eliminate the mixed derivatives of V by choosing a suitable coordinate system xyz such that:

$$V_0^{(2)} = \tfrac{1}{4}(5/\pi)^{1/2} V_{zz}$$

$$V_{\pm 1}^{(2)} = 0 \qquad 2.8$$

$$V_{\pm 2}^{(2)} = \frac{1}{4}(5/6\pi)^{1/2}(V_{xx}-V_{yy})$$

$$= \frac{1}{4}(5/6\pi)^{1/2}\eta V_{zz}$$

where:

$$\eta = \frac{V_{xx}-V_{yy}}{V_{zz}} \qquad 2.9$$

and is a measure of the asymmetry of the crystal structure, i.e., $\eta = 0$ for a structure with axial symmetry. Poisson's equation connecting V_{xx}, V_{yy} and V_{zz} is:

$$V_{xx} + V_{yy} + V_{zz} = 0 \qquad 2.10$$

Thus, by choosing principal axes such that:

$$|V_{xx}| < |V_{yy}| < |V_{zz}|$$

η is restricted to $0<\eta<1$. The gradient tensor is then determined by the parameters V_{zz} and η. In the particular case involving axial symmetry, i.e., with $\eta = 0$, $V^{(2)}$ is given by V_{zz} with:

$$V_{\pm 2}^{(2)} = V_{\pm 1}^{(2)} = 0 \qquad 2.11$$

$$V_0^{(2)} = (5/16\pi)^{1/2} V_{zz}$$

The interaction Hamiltonian then reduces to:

$$K_Q = (\tfrac{1}{5}\pi)^{1/2} T_0^{(2)} V_{zz} \qquad 2.12$$

which, by application of the Wigner-Eckart theorem, can be shown to be diagonal.

Raich and Good[8] show that the angular momentum vector may precess about the directions of strongest or intermediate field gradient but not about that of the weakest and, in particular, for $\eta = 0$ the precession will be about the axis of symmetry.

The definition is made in the literature of the "quadrupole interaction frequency" ω_Q by:

$$\omega_Q = \frac{eQV_{zz}}{4I(2I-1)\hbar} \qquad 2.13$$

where Q is the electric quadrupole moment and I is the spin of the nucleus in the state under investigation. The interaction produces a hyperfine splitting of the energy levels with two-fold degeneracy due to the equivalence of the magnetic quantum numbers +m and -m in a quadrupole interaction. Thus for odd 2I the nuclear energy levels become split into $\frac{1}{2}(2I+1)$ levels and transitions between them occur with characteristic angular frequencies ω_n equal in magnitude to the energy differences divided

by $\hbar$. For $\eta = 0$, the smallest non-vanishing frequency, denoted by ω_0, is equal to $3\omega_Q$ for even 2I and to $6\omega_Q$ for odd 2I. The remaining frequencies are then harmonics of ω_0. The cases for $\eta \neq 0$ are discussed later in the chapter.

For polycrystalline sources with axial symmetry the differential attenuation factor becomes:

$$G_{kk}(t) = \sum_n S_{kn} \cos(n\omega_0 t) \qquad 2.14$$

the S_{kn} depend on the spins involved and are tabulated in reference (4). The summation index n assumes all values of $2|m^2-m'^2|$ for half integer spin. For example, the form of $G_{22}(t)$ for $\eta = 0$ and $I = 5/2$ is shown in Figure 2.1. The limit for the integral attenuation factor for an infinitely strong interaction $G_{kk}(\infty)$ is shown[5] to be:

$$G_{kk}(\infty) = \frac{1}{(2k + 1)} \qquad 2.15$$

and is called the "hard core" value.

In the more complex cases with $\eta \neq 0$ the attenuation factors have been calculated by Matthias et al[7,9] by the diagonalisation of the non-axially symmetric (rhombic) field Hamiltonian and the eigenvalues and eigenfunctions determined for different values of ω_Q

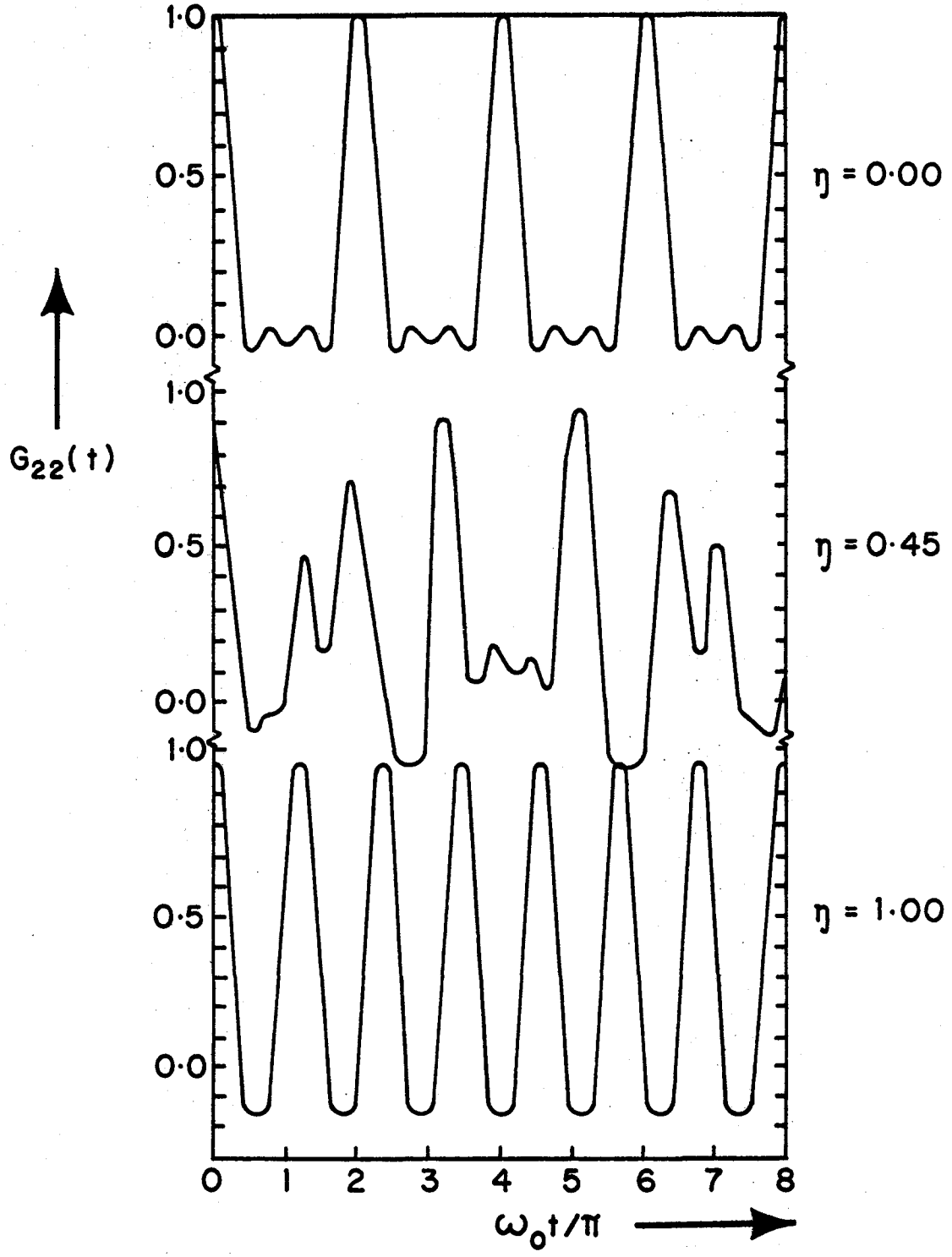

FIGURE 2·1 Differential attenuation function $G_{22}(t)$ for $I = 5/2$ and $\eta = 0{\cdot}00$, $0{\cdot}45$ and $1{\cdot}00$.

and η. Numerical treatments of these cases have also been made by Alder et al[5] and samples of their results are given in Figure 2.1 for several values of η in the case with I = 5/2.

Beraud et al[10] wrote the interaction Hamiltonian for the I = 5/2 case in the form:

$$K_Q = \begin{bmatrix} 10 & 0 & \eta\sqrt{10} & 0 & 0 & 0 \\ 0 & -2 & 0 & \eta\sqrt{18} & 0 & 0 \\ \eta\sqrt{10} & 0 & -8 & 0 & \eta\sqrt{18} & 0 \\ 0 & \eta\sqrt{18} & 0 & -8 & 0 & \eta\sqrt{10} \\ 0 & 0 & \eta\sqrt{18} & 0 & -2 & 0 \\ 0 & 0 & 0 & \eta\sqrt{10} & 0 & 10 \end{bmatrix} \hbar\omega_Q \qquad 2.16$$

which on diagonalization realises the Cardano type equation for the energy splitting W in units of $\hbar\omega_Q$:

$$W^3 - 28W(\eta^2 + 3) + 160(\eta^2 - 1) = 0 \qquad 2.17$$

Solving this cubic equation for various values of η enables one to find the eigenvalues shown in Figure 2.2 and hence obtain the three frequencies ω_0, ω_1 and ω_2 involved in an I = 5/2 quadrupole splitting in terms of ω_Q. In Figures 2.3 and 2.4 are plotted the ratios ω_0/ω_Q and ω_1/ω_0 as functions of η. Reference to Figure 2.2 will show that the three frequencies are not independant as $\omega_0 + \omega_1 = \omega_2$, or $\omega_2/\omega_0 = \omega_1/\omega_0 + 1$. Thus measurements of ω_0, ω_1 and ω_2 are a handle on the important asymmetry factor of η of the crystal environment. Beraud et al[10]

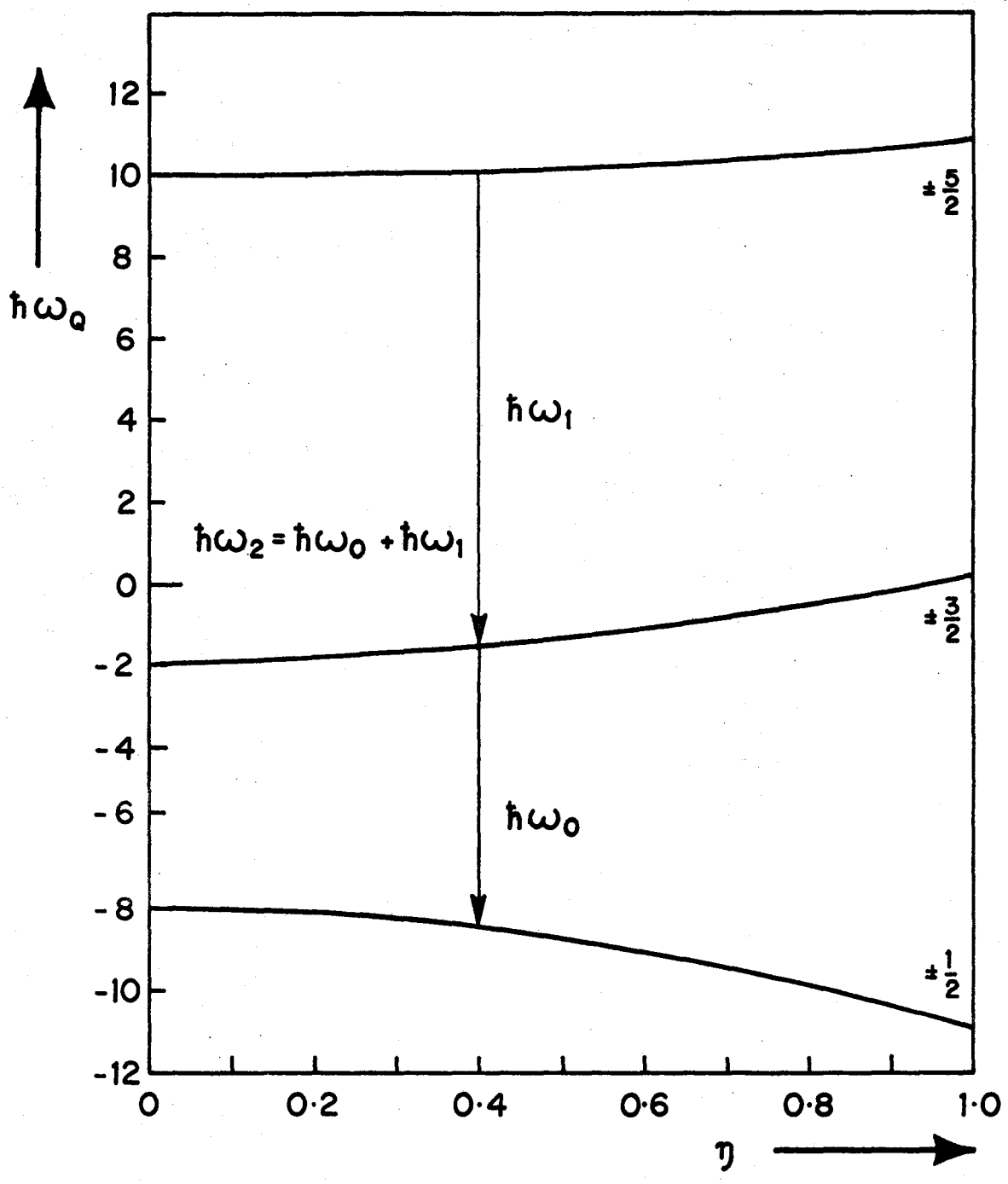

FIGURE 2·2 The splitting of a spin $^{5}/_{2}$ level by a quadrupole interaction as a function of η

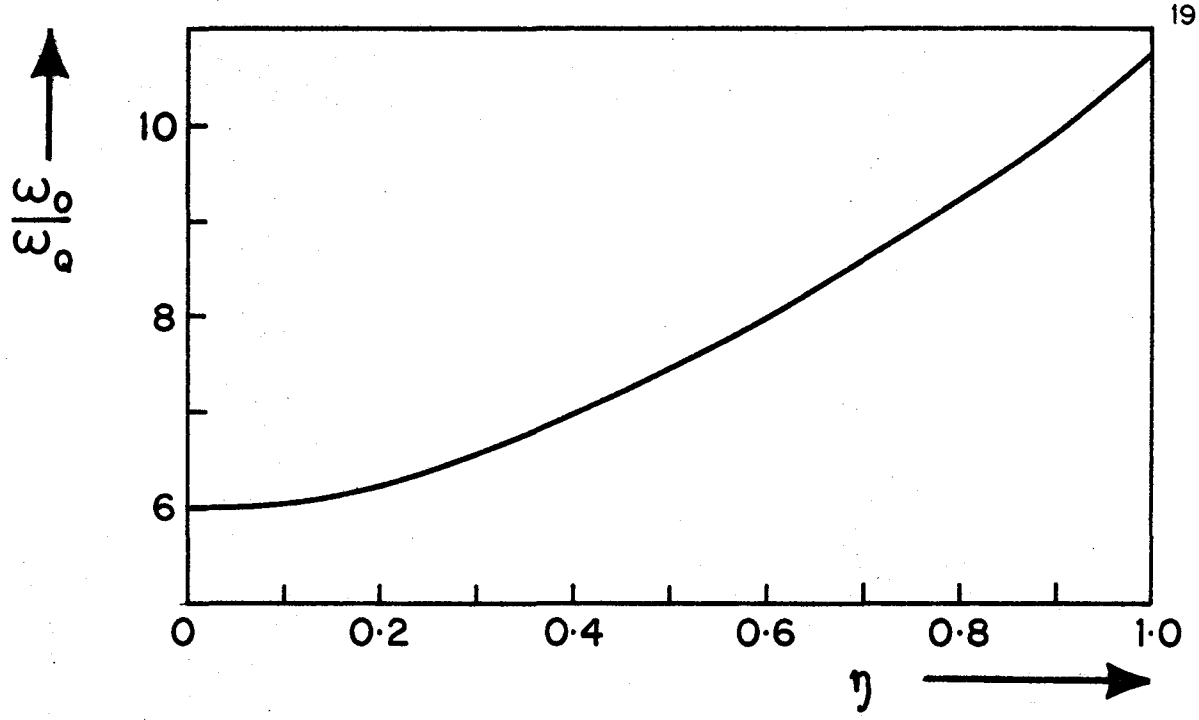

FIGURE 2·3 A plot of ω_0 / ω_Q against η

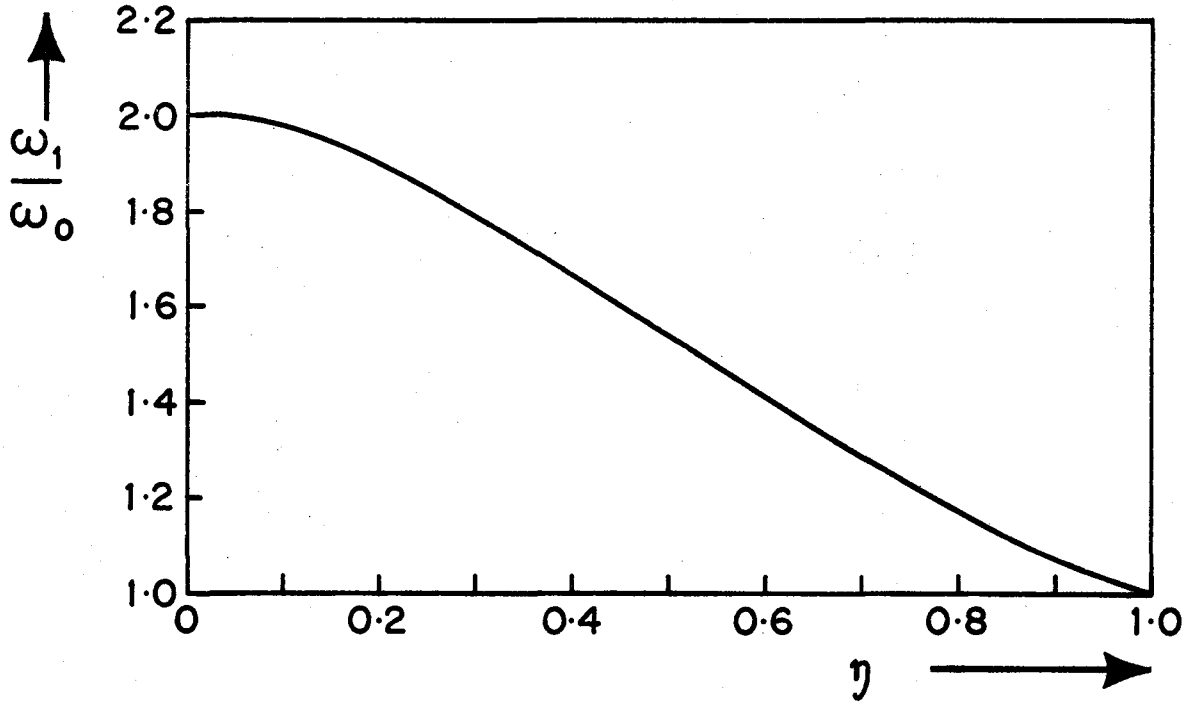

FIGURE 2·4 A plot of ω_1 / ω_0 against η

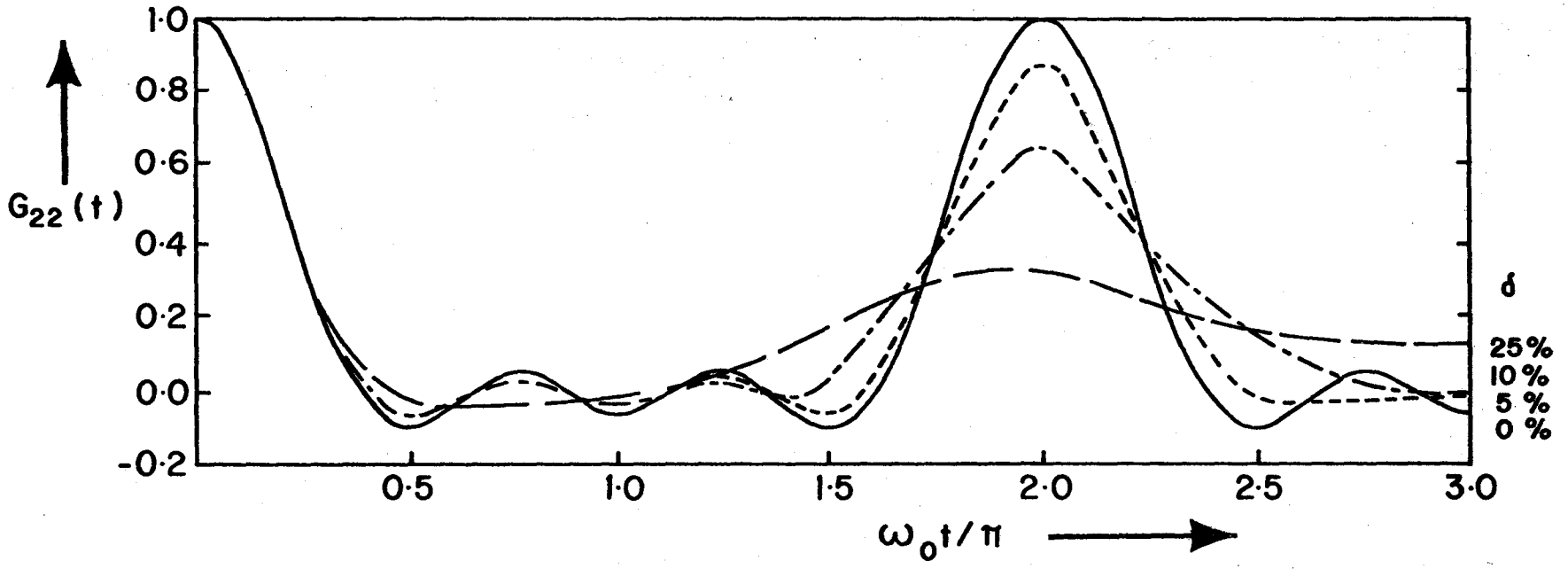

FIGURE 2·5 . The effect on $G_{22}(t)$ of a normal frequency distribution of varying width δ.

also calculated the amplitudes of the 3 frequencies for the I = 5/2 case as a function of η, thus giving a check on a measurement of η. A single measurement of ω_0 on the other hand would only give the product QV_{zz} from Equation 2.13.

2.2 THE EFFECT OF A DISTRIBUTION OF FREQUENCIES

This is considered by Alder et al[5] who released the assumption that the electric field gradient is exactly the same at different crystal sites. Frequency distributions may also arise from lattice defects produced by nuclear recoil following irradiation by a neutron beam, placing active nuclei in a distribution of lattice sites. Their results show, as in Figure 2.5, the effect on $G_{22}(t)$ of normal frequency distributions with varying relative width δ.

This has some importance when applied to crystals with cubic symmetry at the lattice sites in which the field gradients should vanish, eliminating the quadrupole interaction. However, lattice imperfections and recoil effects will introduce lattice site displacements, and hence subject active nuclei to non-vanishing field gradients; and then a definite quadrupole interaction may, in fact, be seen to be present.

CHAPTER 3

INSTRUMENTAL EFFECTS INVOLVED IN THE MEASUREMENT OF DIFFERENTIAL PERTURBED ANGULAR CORRELATIONS

The details of the experimental arrangements actually used in this work are described in Chapters 6 and 7, and what follows here is a theoretical treatment of some instrumental effects encountered during PAC measurements.

The basic experimental setup follows that described in Chapter 1 but involves the measurement of $W(\theta,t)$, instead of just $W(\theta)$ described there, for two angles, 90 and 180 degrees. $G_{22}(t)$ is then obtained using equation 2.3 by neglecting terms of order higher than second with the justification mentioned in the next section.

$W(\theta,t)$ is obtained by measuring the coincidence rate of, say, γ_1 and γ_2 in Figure 1.2, as a function of the time difference between the emissions of γ_1 and γ_2, i.e., between the times of formation and decay of the intermediate level b. This is achieved by a "time to amplitude converter" (TAC) which is basically

a clock which is started by pulses corresponding to γ_1 and stopped by those corresponding to γ_2 by having a coincidence circuit which only takes the outputs from the TAC, i.e., voltage pulses of height proportional to the time interval, when coincidences corresponding to γ_1 being received in counter 1 and γ_2 in counter 2 are achieved. All other "starts and stops" being generated by the TAC are then rejected. The pulses are then stored in a pulse height analyzer.

This type of system is frequently used to measure the lifetimes of excited nuclear states, e.g. see Reference 11, and is adapted here to study the form of $W(\theta,t)$. Such a system has a finite time resolution τ, i.e., if two simultaneously emitted gamma rays are received in counters 1 and 2 the form of the distribution of voltage pulses from the TAC, as stored in the analyzer, would be a δ function at a position corresponding to zero time, if the time resolution was perfect: that is, a δ function also. However, the electronics and spatial dimensions of the detectors place lower limits on τ and the "prompt" curve obtained from two simultaneously emitted gamma rays will always have a finite width at half maximum height (FWHM); and τ is assigned this value. τ depends largely on the type of detectors used and on the energies of γ_1 and γ_2. In this work the lowest value of τ was 1.3 nsec.

3.1 THE EFFECT OF FINITE TIME RESOLUTION ON A PAC MEASUREMENT

This is treated by Beraud et al[10] who calculated analytically the distortion of a differential perturbed angular correlation paying special attention to a level with spin 5/2. Basically one can say that if the characteristic frequencies ω_n involved in the interaction are of the order of magnitude $1/\tau$, where τ is the time resolution of the system, the measured attenuation factor becomes:

$$\left\langle G_k(t)\right\rangle_\tau = \frac{\int_0^\infty P(t-t')\exp(-\lambda t')G_k(t')dt'}{\int_0^\infty P(t-t')\exp(-\lambda t')dt'} \qquad 3.1$$

where $P(t-t')$ is the response function of the system, supposedly with a normal form. The effect of the finite time resolution on the measurement of the ω_n is discussed in Chapter 4 and it suffices here to say that the effect is a dampening down of the oscillation amplitudes of the frequencies by the factor $\exp(-1/2\omega_n{}^2\tau^2)$. Beraud et al have calculated the forms of $G_{22}(t)$ for various time resolutions and values of η for the spin 5/2 case and an example for $\eta = 0.5$ is shown in Figure 3.1.

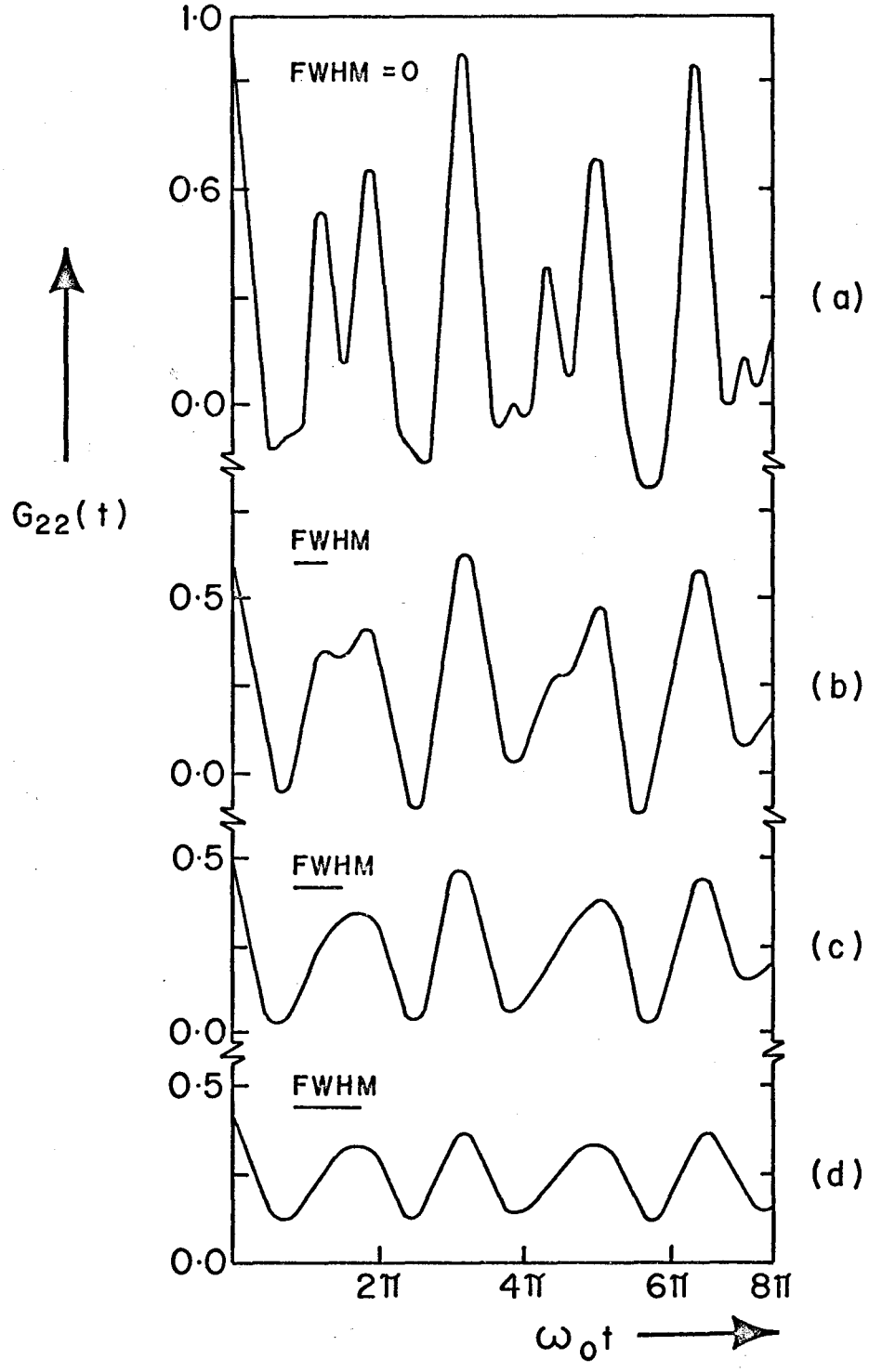

FIGURE 3·1 The effect of various time resolutions on $G_{22}(t)$ for $\eta = 0{\cdot}5$

It can be appreciated from the above that if good measurements of the ω_n are desired then a small time resolution (compared to $2\pi/\omega_{max}$) is essential, as the higher frequencies will be strongly attenuated by the effects of the finite time resolution.

3.2 THE EFFECT OF FINITE SOLID ANGLES SUBTENDED BY THE DETECTORS AT THE SOURCE

The detectors 1 and 2 of Figure 1.2 subtend finite solid angles at the source. This has two main effects on the data, one enhancing, and the other degrading the observed magnitude of the effects under investigation. The enhancement comes from the simple fact that the count rate in a detector is proportional to the solid angle subtended at the source and so a large solid angle will tend to improve the statistical nature of the data for a given counting time.

However, the finite solid angle tends to wash out the angular dependence of $W(\theta,t)$ and what follows is an attempt to find an optimum value in order to balance the above effects. The A_{kk} in Equation 2.1 become progressively smaller with increasing order and so, for a first approximation, we write $W(\theta)$ as:

$$W(\theta) = 1 + A_2 P_2(\cos\theta) \qquad 3.3$$

$$= 1 + \frac{3\cos^2\theta - 1)}{2}$$

writing: $\cos^2\theta = \frac{1 + \cos 2\theta}{2}$

gives: $W(\theta) = B + C\cos 2\theta \qquad 3.4$

The measured angular correlation function $W'(\theta)$ will be:

$$W'(\theta) = \int W(\theta')R(\theta - \theta')d\theta' \qquad 3.5$$

where $R(\theta - \theta')$ is the solid angle effect and may be expressed (assuming 100 per cent efficiency) as:

$$R(\theta - \theta) = \frac{1}{2\Delta} \quad \theta' - \Delta \leqslant \theta \leqslant \theta' + \Delta \qquad 3.6$$

$$= 0 \quad |\theta - \theta'| > \Delta$$

Thus $R(\theta - \theta')$ is a rectangular function of width 2Δ and height $1/2\Delta$ (and hence unit area) as shown in Figure 3.2 where Δ is the half angle shown in Figure 3.3.

Then $W'(\theta)$ becomes:

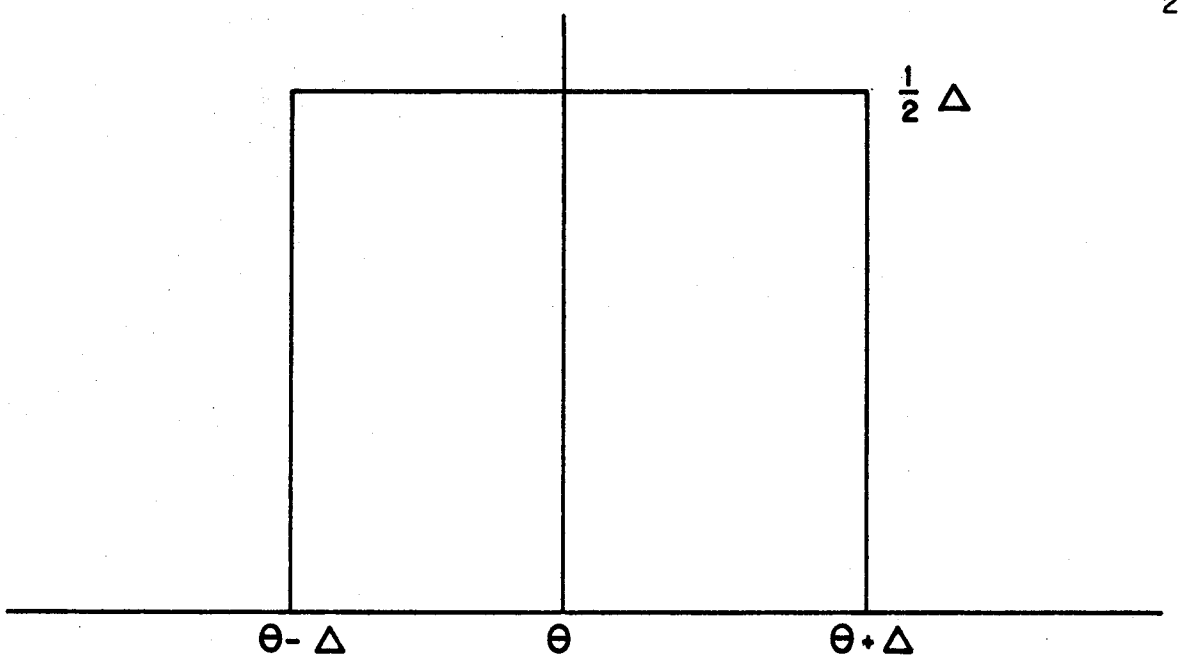

FIGURE 3·2 The rectangular solid angle effect function

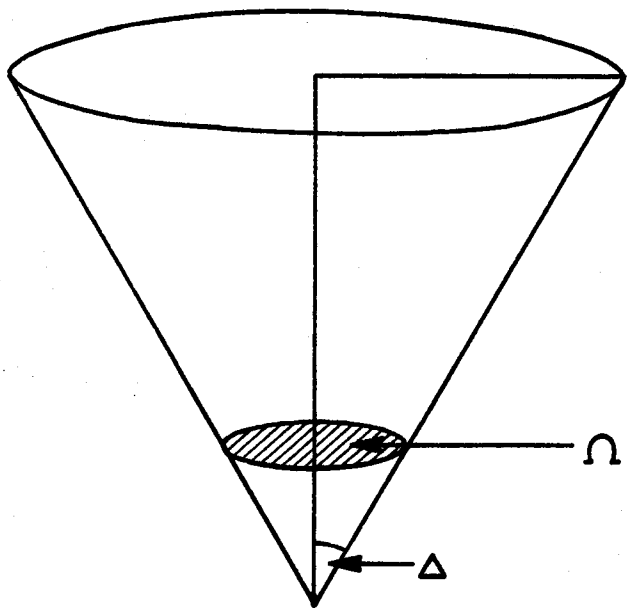

FIGURE 3·3 The angles involved in the solid angle effect.

$$W'(\theta) = \frac{1}{2\Delta}\int_{\theta-\Delta}^{\theta+\Delta}(B + C\cos 2\theta')d\theta' \qquad 3.7$$

$$= \frac{1}{2\Delta}\left[B\theta' + \frac{C}{2}\sin 2\theta'\right]_{\theta-\Delta}^{\theta+\Delta}$$

$$= \frac{1}{2\Delta}\left(B\theta + B\Delta - B\theta + B\Delta\right) + \frac{C}{4\Delta}\sin 2(\theta + \Delta) - \frac{C}{4\Delta}\sin 2(\theta - \Delta)$$

$$= B + \frac{C}{4\Delta}(2\sin 2\Delta\cos 2\theta)$$

$$= B + \frac{C}{2\Delta}\sin 2\Delta\cos 2\theta \qquad 3.8$$

Thus, by comparing equations 3.4 and 3.8, we can see that the effect of the finite solid angle is to degrade the angular dependence of $W(\theta)$ by a factor $\frac{\sin 2\Delta}{2\Delta}$ for each counter. This effect will become more pronounced for higher order terms A_{kk} because Δ becomes $k\Delta$ in the above discussion and so we have additional justification for ignoring them in a reasonable approximation of $W(\theta)$.

The count rate is proportional to the solid angle subtended at the source. Designating this by Ω as in Figure 3.3, we have, in polar coordinates:

$$d\Omega = \sin\theta d\theta d\phi$$

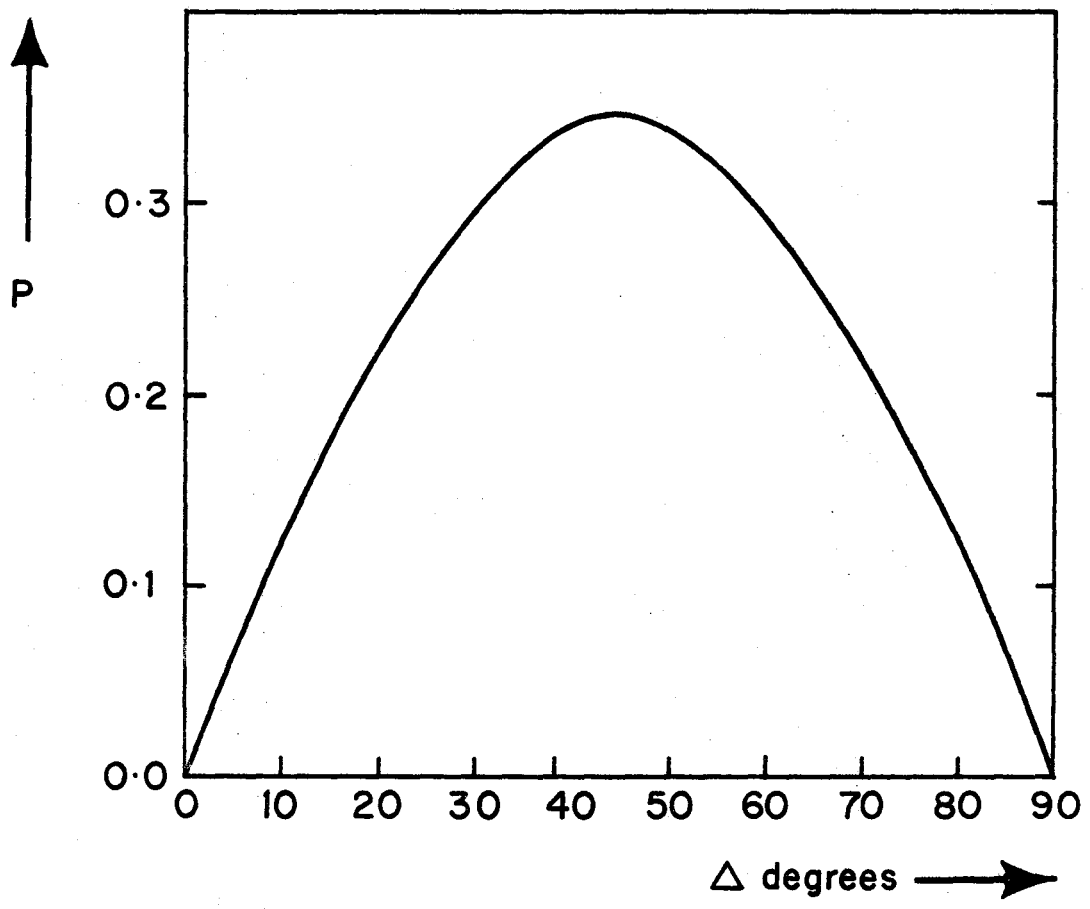

FIGURE 3·4 The variation of the solid angle effect P with half angle Δ.

Thus:

$$\Omega = -2\pi \int_0^{\Delta} \sin\theta d\theta$$

$$= \left[2\pi \cos\theta \right]_0^{\Delta}$$

$$= 2\pi(1 - \cos\Delta)$$

or as a fraction of π $= 1/2(1 - \cos\Delta)$

So for optimum efficiency we must maximize the product p of the square root of the count rate effect factor (as the statistical uncertainties are inversely proportional to the square root of the count) and the angular degradation factor,

i.e.: $$P = (1 - \cos\Delta)^{1/2} \operatorname{sinc} 2\Delta$$

P is plotted in Figure 3.4 and shows the optimum solid angle is one corresponding to a Δ of about 45 degrees.

CHAPTER 4

THE ANALYSIS OF THE $G_{22}(t)$ USING FOURIER TRANSFORM METHODS

Fourier transforms play important parts in many branches of science and are more than just mathematical functions or methods, but are concrete physical relationships between measureable physical entities. The most important such relationship from the point of view of this work is the fact that any spectrum, i.e., the distribution of intensities as a function of frequency, is a Fourier transform of a waveform, that is, an oscillation amplitude varying with time. We obtain a type of waveform when we measure the $G_{22}(t)$ attenuation function as pictured in Figure 2.1 and we will use Fourier transform methods to extract the frequencies contained in that function.

The theory and uses of Fourier transforms are well described in Reference (12) and here only a few relevant outlines are sketched. The Fourier transform F(s) of a function f(x) is defined as:

$$F(s) = \int_{-\infty}^{\infty} f(x)\, e^{-2\pi i x s} dx \qquad 4.1$$

If we transform F(s) by the same formula we obtain:

$$f(w) = \int_{-\infty}^{\infty} F(s)\ e^{-2\pi iws} ds$$

If f(x) is an even function of x the repeated transformation will yield f(w), the origonal function. Thus Fourier transformations have a cyclic property and as 2 steps are involved the reciprocal property is implied, i.e., if F(s) is the Fourier transform of f(x) then f(x) is the Fourier transform of F(s).

Symmetry properties play important roles in Fourier transforms, as when f(x) is an odd function the repeated transformation will yield f(-w). Symmetry will be discussed further later on. The customary formulas exhibiting the reversibility of the Fourier transform are:

$$F(s) = \int_{-\infty}^{\infty} f(x)\ e^{-2\pi ixs} dx$$

$$f(x) = \int_{-\infty}^{\infty} F(x)\ e^{2\pi ixs} ds \qquad 4.2$$

These may be expressed as a repeated integral:

$$f(x) = \int_{-\infty}^{\infty} \left[\int_{-\infty}^{\infty} f(x)\ e^{-2\pi ixs} dx \right] e^{2\pi ixs} ds \qquad 4.3$$

4.1 CONDITIONS FOR THE EXISTENCE OF FOURIER TRANSFORMS

If a function is an accurately specified description of a physical quantity then its Fourier transform must exist. However, this is rarely the case in the simple mathematical expressions that are often substituted for these quantities. For instance, the sine function is often used to represent a waveform but for it to do so completely it would have to have been switched on an infinite time ago. Frequently used mathematical functions which are good approximations to physical entities strictly speaking do not have Fourier transforms, i.e., the Fourier integral of Equation 4.3 does not converge for all s for these functions.

For that equation to be convergent the following conditions must apply:

1. The integral of f(x) must exist from ∞ to $-\infty$.
2. Any discontinuities in f(x) must be finite, although the use of limits may, in certain cases, avoid this difficulty.
3. The number of maxima or minima of f(x) must be finite. This excludes functions like $\sin\frac{1}{x}$ in a range including zero.

Just because many common functions do not have Fourier transforms in the ordinary sense it does not necessarily

detract from their usefulness, as they can be treated by the generalization of Fourier transforms "in the limit".

For example, a periodic function P(x) does not have a Fourier transform but it does have a spectrum which can be identified with the coefficients of its Fourier series. We may modify P(x) by a factor $e^{-\alpha x^2}$ where α is a small positive number such that $e^{-\alpha x^2} P(x)$ does possess a Fourier transform; then, by making α approach zero producing a series of functions with a series of transforms, the limit of the latter will form a generalised function which will be a Fourier transform of P(x).

4.2 SYMMETRY IN FOURIER TRANSFORMS

Any function can be split into a sum of even and odd parts, i.e.:

$$f(x) = E(x) + O(x) \qquad 4.4$$

One can show that:

$$E(x) = \frac{1}{2} (f(x) + f(-x))$$

$$O(x) = \frac{1}{2} (f(x) - f(-x))$$

Both E(x) and O(x) may be complex. In terms of them the Fourier transform of f(x) then reduces to:

$$F(s) = 2\int_0^\infty E(x)\cos(2\pi xs)dx - 2i\int_0^\infty O(x)\sin(2\pi xs)dx \qquad 4.5$$

The cosine transform of f(x) is defined as:

$$F_c(s) = 2\int_0^\infty f(x)\cos(2\pi xs)dx \qquad 4.6$$

The cosine transform can be regarded, from equations 4.5 and 4.6, to be the Fourier transform of the even part of f(x). The cosine transform is exactly reversible, i.e.:

$$f(x) = 2\int_0^\infty F_c(s)\cos(2\pi sx)\,ds$$

The sine transform of f(x) is:

$$F_s(s) = 2\int_0^\infty f(x)\sin(2\pi xs)dx \qquad 4.7$$

and is i times the odd part of f(x). The Fourier transform of the whole of f(x) is then the Fourier transform of E(x) plus i times the Fourier transform of O(x). If we take the sum of the squares of $F_c(\omega)$ and $F_s(\omega)$ for a waveform f(t) we may then call the result the "power spectrum" $|F(\omega)|^2$ of the waveform, i.e., the distribution

of power as a function of frequency. This is the quantity we shall examine in the case of $G_{22}(t)$ in order to find the frequency components contained in it.

4.3 THE CONVOLUTION THEOREM

"Convolution" always appears when a physical quantity is measured with an instrument possessing a finite resolution. The response function of the instrument is convolved with or "folded into" the true data to give the measured data. It can be demonstrated physically and mathematically that such convolution results in the smoothing or smearing out, of the structure of the actual data. The convolution of two functions f(x) and g(x) is:

$$h(x) = \int_{-\infty}^{\infty} f(u)g(x-u)du \qquad 4.8$$

or simply:

$$h(x) = f(x)*g(x)$$

The convolution theorem may be stated as follows: "If f(x) has the Fourier transform F(s), and g(x) has the Fourier

transform F(s)G(s); i.e., convolution of two functions means multiplication of their transforms."

This may be derived as follows:

$$\int_{-\infty}^{\infty}\int_{-\infty}^{\infty}\left[f(x')g(x-x')dx'\right]\exp(-i2\pi xs)dx$$

$$= \int_{-\infty}^{\infty} f(x')\left[\int_{-\infty}^{\infty} g(x-x')\exp(-2\pi ixs)dx\right]dx'$$

$$= \int_{-\infty}^{\infty} f(x')\exp(-2\pi ix's)G(s)dx'$$

$$= F(x)G(s) \qquad 4.9$$

The converse of the above also holds, i.e., the transform of a product is the convolution of the transforms.

The following properties follow directly from the above theorem:

1. The area under a convolution is equal to the product of the areas under the factors.

2. The abscissas of the centres of gravity add.

3. The variances of the factors add in the transform.

The convolution of a function with itself is called the "auto-correlation" function. By putting f(x) = g(x) in the above arguments we see that the power spectrum

of f(x) is the Fourier transform of its auto-correlation function.

4.4 APPLICATION OF THE CONVOLUTION THEOREM TO THE ANALYSIS OF $G_{22}(t)$

We now apply the aforegoing ideas to the analysis of the frequencies contained in the measured $G_{22}(t)$ attenuation function. If we had a sample representing an infinitely long time period and with perfect statistics we would expect the power spectrum of $G_{22}(t)$ to be sharp peaks at frequencies corresponding to the ω_n; but the following instrumental effects, some of which were discussed in Chapter 3, are contained in the data which transfer themselves into the power spectrum through the principles expressed in the convolution theorem.

1. Because of the exponential decay of the nuclear level under investigation one can only look at the form of $G_{22}(t)$ over a finite time interval, which in our case extends over from 25 to 35 nsec. This is equivalent to multiplying the data by a rectangular function $\Pi(t)$ where:

$$\Pi(t) = 1 \quad 0 \leqslant t \leqslant t' \qquad 4.10$$
$$= 0 \quad t > t'$$

and t' is the time interval being used. This results in the convolution of the power spectrum of such a

rectangular function with that of the data. The Fourier transform of a rectangular function $\Pi(t)$ is:

$$F(\omega) = \frac{\sin\pi\omega t'}{\pi\omega t'} \qquad 4.11$$

$$= \text{sinc}\omega t'$$

and its modulus squared is:

$$|F(\omega)|^2 = \text{sinc}^2\omega t' \qquad 4.12$$

The form of this function convolved with the power spectrum of a cosine function with an oscillation frequency of 823 Mrad/sec and representing a time interval of 25 nsec is shown in Figure 4.1 where it can be seen that its effect is to broaden the peak at 823 Mrad/sec and give it small side peaks. The effect is analagous to the intensity distribution resulting from Fraunhofer diffraction of light passing through an infinitely long narrow slit which can also be described by a rectangular function $\Pi(x)$. The width of the peak due to the finite time interval t' as measured in frequency is given approximately by $1/t'$. Thus it can be seen that it is advantageous to use as long a time interval as possible in order to minimise the broadening of the power spectrum peaks. The above calculation also serves as a test of the method of analysis.

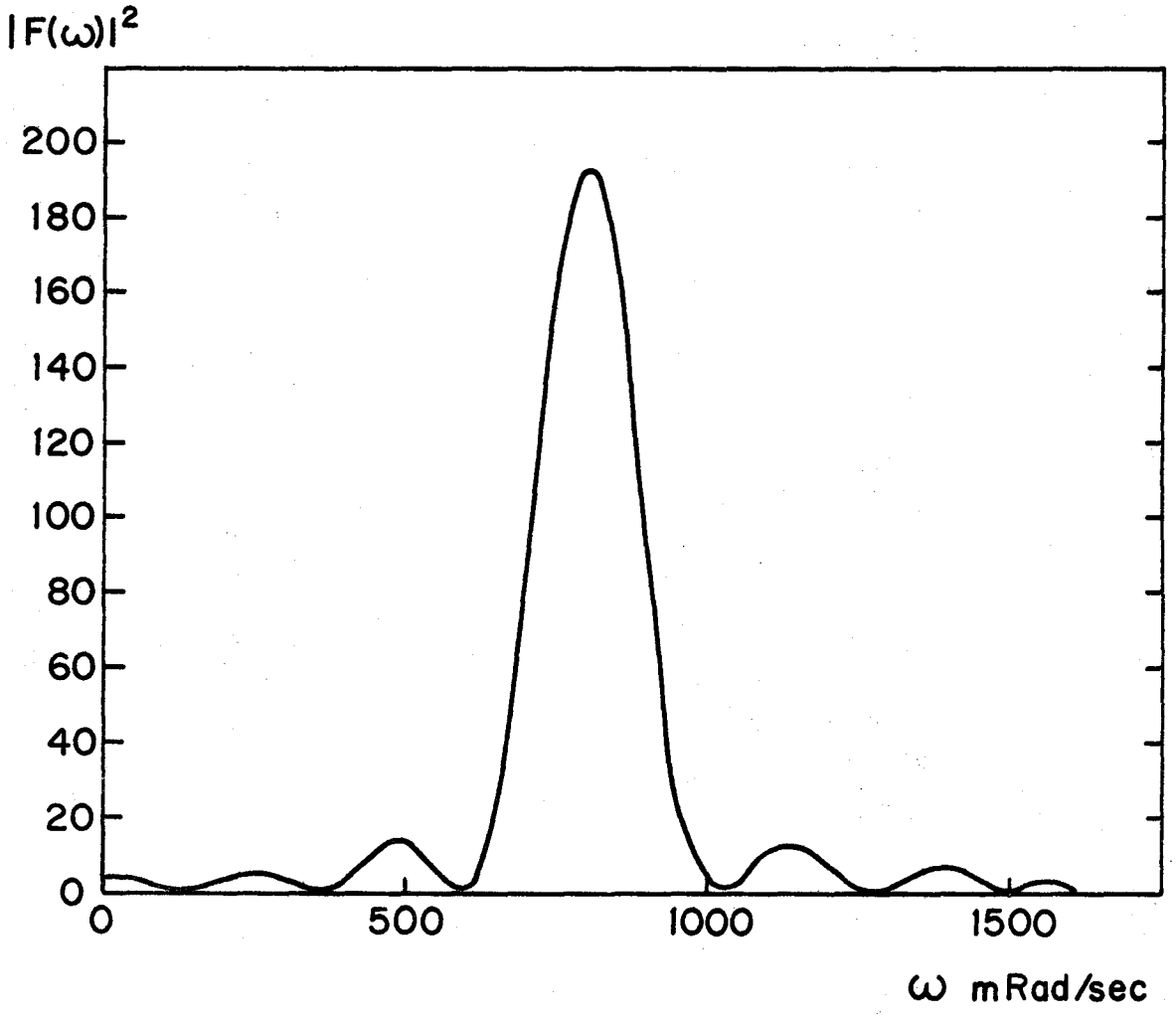

FIGURE 4·1 The broadening of an 823 mRad/sec oscillation power spectrum peak by a finite time interval of 25 n sec.

2. The time dependence of $G_{22}(t)$ is obtained from E(t) which is represented by distributions of pulse heights from the TAC, as stored in a pulse height analyzer which counts the number of pulses falling in small voltage intervals as represented by the channels of the analyzer according to the time scale calibration. Thus the form of E(t) is discrete in both the E and t variables. Although the former discreteness may be neglected, the second has several important effects. Firstly, it sets an upper limit on any frequency that can be measured with such a system, as any complete cycle of oscillation would have to be represented by at least three channels. If the time scale calibration is c sec per channel the maximum measureable frequency would be about 1/3c. In our case a time scale calibration of about 0.5 nsec per channel was used, which yields an upper limit of about 600 MHz. The second effect is that the finite mesh size of the time scale may introduce uncertainties in the centroid positions of the power spectrum peaks, i.e., the centroid positions may only correspond to the true frequencies for completely smooth data. These and similar effects are to be subjected to further study.

3. The data contains statistical spread and this affects the power spectrum by adding a "white noise"

contribution, which is evenly distributed along the baseline among all frequencies up to the cutoff due to the finite channel width. The statistical noise is not, of course, constant but increases with time as the level decays, and its effect is to impose the finite time interval as discussed earlier. The great advantage in using Fourier transform methods to analyze data of this kind is that one obtains a considerable increase in the signal to noise ratio in the power spectrum as compared to the data because, as Equation 4.7 shows, each point in the power spectrum is obtained using the information contained in every point in the time dependant function. This principle is called "Fellget's advantage" and it can be shown that the gain is given by $m^{1/2}$, where m is the number of elements in the time dependency.

4. The measured $G_{22}(t)$ function is a convolution of the actual function and the time response function of the system as described in Chapter 2. The latter is approximately a gaussian of FWHM τ, with the form $R(t) = \exp(-2t^2/\tau^2)$. The Fourier transform of a gaussian function is also a gaussian and so each point in the power spectrum of $G_{22}(t)$ is multiplied by the factor $\exp(-\omega_n{}^2\tau^2_{/2})$. Thus all the heights of the peaks are degraded by this factor, making the higher frequencies increasingly difficult to determine. The finite time resolution also sets an upper limit on the measureable frequencies as no frequency can be

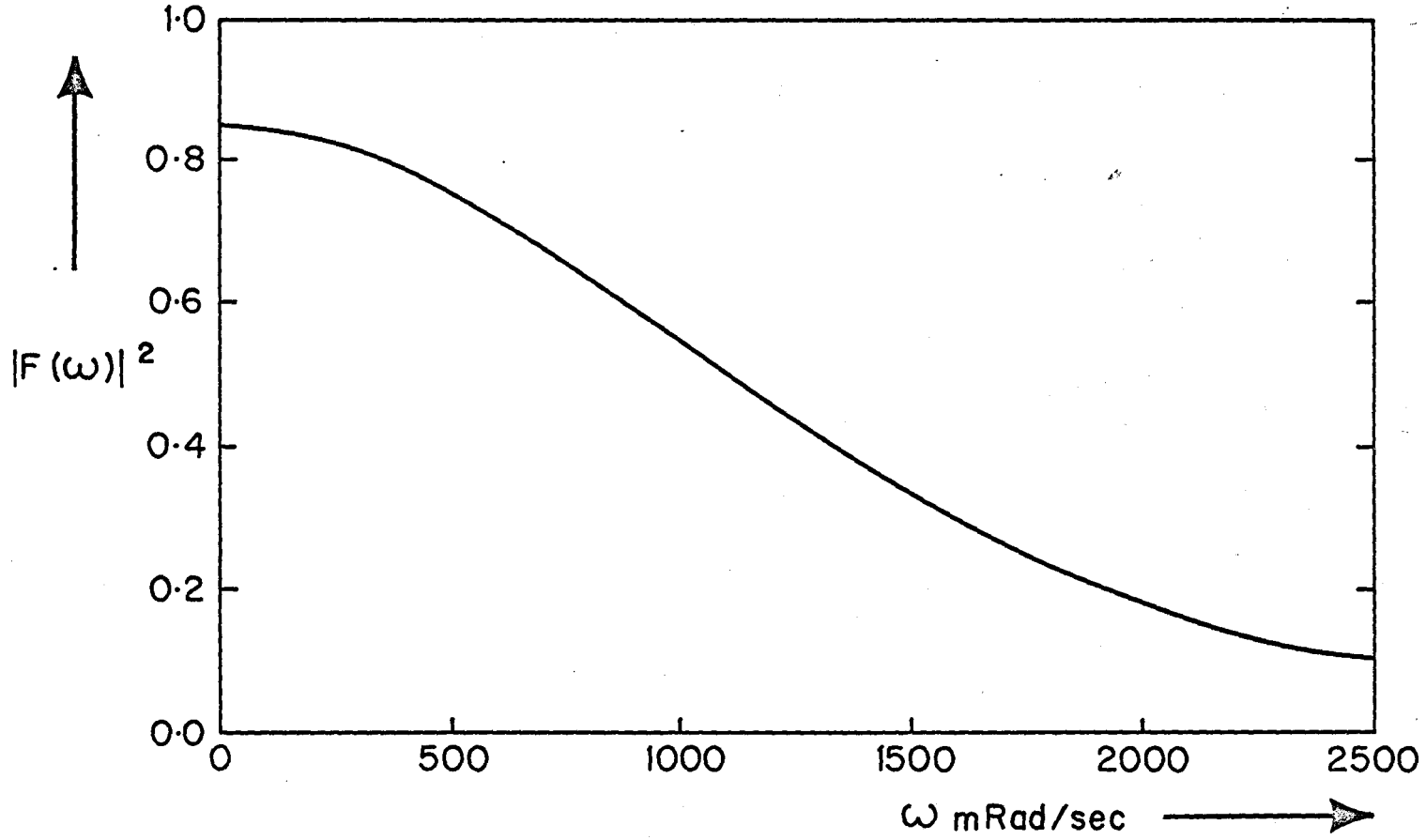

FIGURE 4·2 The power spectrum of a measured time response with FWHM of 1·3 n sec.

resolved having a period smaller than τ. The power spectrum of the 1.3 nsec time response curve of Figure 7.3 is depicted in Figure 4.2.

5. Solid angle effects tend to wash out the angular structure of $G_{22}(t)$ through Equation 3.8 diminishing all the power spectrum peaks by equal proportions.

6. The peaks will also contain some broadening due to the frequency distribution effects described in Chapter 2.

CHAPTER 5

THE APPLICATION OF PAC MEASUREMENTS TO Ta^{181} NUCLEI IN VARIOUS CRYSTAL ENVIRONMENTS

Hf^{181} decays to Ta^{181} via the decay scheme[13] shown in Figure 5.1. The 133-482 KeV cascade in Ta^{181} lends itself to the study of electric quadrupole interactions for several reasons:

1. Ta^{181} is a highly distorted nucleus with a relatively large quadrupole moment of $2.53 \pm 0.10 \times 10^{-24}$ cm^2 for the 482 KeV level[14].

2. The 482 KeV level with spin 5/2 follows strongly from the 615 KeV level which, with its long lifetime of 17.6 μsec, allows the decay of the positive charge of the Ta^{181} atoms following the beta decay of Hf^{181}. In conductors this process is extremely rapid, within 10^{-12} sec, but takes a time in the order of 10^{-8} sec in the case of insulators. Any such electrostatic effects present during the lifetime of the 482 KeV level would seriously influence the angular correlation of the 133-482 KeV cascade.

3. The half-life of the 482 KeV level is 10.6 nsec which is sufficiently long to allow several complete

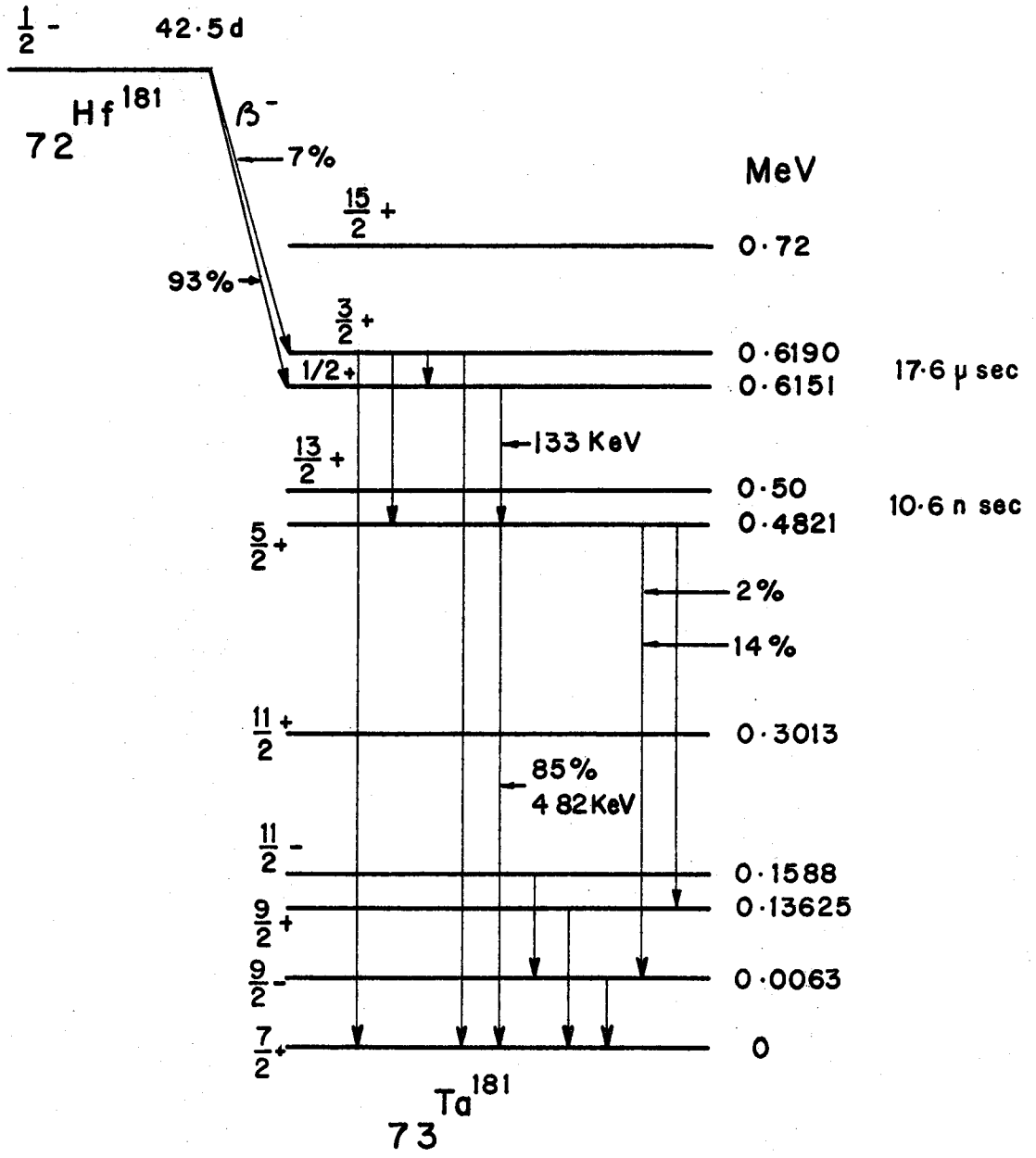

FIGURE 5·1 The decay of Hf^{181}

quadrupole precessions to be followed during the course of a measurement.

4. Only one long lived isotope of hafnium exists with a high neutron cross-section, i.e. Hf^{181} which enables one to study just one isotope of Ta ; namely Ta^{181}.

Differential studies have been made of the quadrupole interactions of Ta^{181} in Hafnium metal crystals by Ouseph and Canavan[15,16], and Sommerfeldt and Schecter[17]. Salomon et al[18] investigated the temperature dependence of the effect in hafnium metal. They also studied[19] the quadrupole interactions of Ta^{181} in $HfAl_2$, HfAl and HfO_2 crystal environments. In this last case they found a very strong perturbation lasting about 5 nsec after which no perturbation occurred. Marest et al[20] also studied the quadrupole interactions of Ta^{181} in HfO_2 and found quite different effects: their results showed a static interaction and they were able to extract the fundamental frequency ω_0 described in Chapter 2, which they assigned the value 780 ± 70 Mrad/sec. Using this value of ω_0 and the above value for the qudrupole moment they found the absolute value of the electric field gradient to be $13.4 \pm 1.2 \times 10^{17}$ V/cm^2.

Gerdau et al[21] have undertaken a detailed study of the quadrupole interactions of Ta^{181} in various

compounds including HfO_2; their results for HfO_2 are summarized as follows:

$\omega_0 = 857 \pm 8$ Mrad/sec $\quad\quad \omega_1 = 1469 \pm 19$ Mrad/sec

$\omega_2 = 2405 \pm 110$ Mrad/sec $\quad\quad \omega_Q = 125.5 \pm 2.5$ Mrad/sec

$\eta = 0.37 \pm 0.03$ Mrad/sec $\quad\quad V_{zz} = 13.1 \pm 0.6 \times 10^{17}$ Vcm^{-2}

These results were for a unannealed sample, small changes occurred after annealing.

5.1 THE STRUCTURE OF HAFNIUM OXIDE

Early studies[22] of the structure of HfO_2 gave it as being cubic, but later reports[23,24] indicated that it was monoclinic and very similar to that of ZrO_2, but with the lattice constants:

$a = 5.1156 \pm 0.005$ Å $\quad\quad b = 5.1722 \pm 0.0005$ Å

$c = 5.1948 \pm 0.005$ Å $\quad\quad \beta = 99^0\,11' \pm 0^0\,05'$

This structure is shown in Figure 5.2. There are four molecules per unit cell and the positions of the hafnium atoms in the unit cell ensure that each hafnium atom experiences the same environment, and thus a unique value for η.

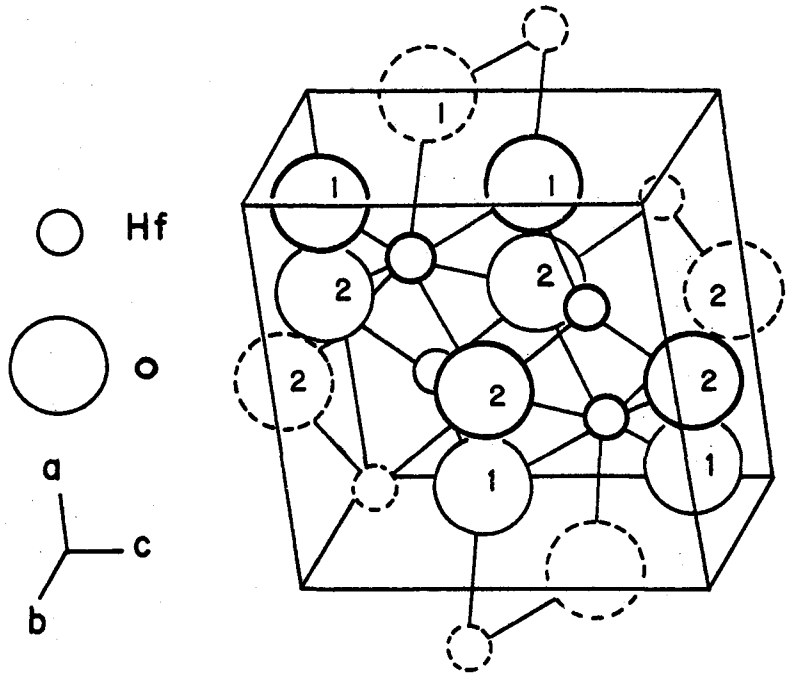

FIGURE 5·2 The structure of HfO_2

Baun[25] studied the temperature dependence of the structure for pure HfO_2 and found that it undergoes a phase transformation from monoclinic to tetragonal between 1800 and 1900 K. On cooling the tetragonal phase is stable until about 1750-1850 K when the monoclinic form is regained. The addition of impurities will drastically lower the transformation temperature, by up to as much as 400 kelvins in the case of very impure samples.

Even when a particular crystal structure is known, the calculation of the electric field gradients and the asymmetry parameter η at active lattice sites is very difficult, and PAC methods are one of the few ways of achieving a measurement of η.

If HfO_2 were cubic there would be no perturbation of the angular correlations of the cascades of Ta^{181} in a perfect lattice, as the field gradients would vanish at the active lattice sites as a result of the cubic symmetry. However, lattice defects and recoil effects would give rise to small non-zero perturbations, but the magnitude of the effects found in this work as shown in Chapters 8 and 9 clearly eliminate such a structure.

5.2 THE ANGULAR CORRELATION OF THE 133-482 KeV CASCADE IN Ta^{181}

Writing the unperturbed angular correlation

function up to order 4 gives:

$$W(\theta) = 1 + A_{22}P_2(\cos\theta) + A_{44}P_4(\cos\theta) \qquad 5.1$$

The Ferentz-Rosenzweig tables give the unperturbed coefficients as: $A_{22} = -0.297$ and $A_{44} = -0.071$. A_{44} will be diminished by the solid angle effects discussed in Chapter 3 and is henceforth neglected. The perturbed angular correlation function then becomes:

$$W(\theta,t) = 1 - 0.297G_{22}(t)P_2(\cos\theta) \qquad 5.2$$

We obtain $G_{22}(t)$ through the ratio:

$$E(t) = \frac{W(\pi,t)}{W(\frac{\pi}{2},t)} = \frac{1 + 0.297\left[3\cos^2(\pi) - 1\right]G_{22}(t)/2}{1 + 0.297\left[3\cos^2(\frac{\pi}{2}) - 1\right]G_{22}(t)/2} \qquad 5.3$$

$$= \frac{1 - 0.197G_{22}(t)}{1 + 0.149\,G_{22}(t)}$$

making:

$$G_{22}(t) = \frac{1 - E(t)}{0.149(E(t) + 2)} \qquad 5.4$$

Equation 5.4 is the one used to obtain the form of $G_{22}(t)$ from measurements of E(t).

CHAPTER 6

FACTORS AFFECTING THE TIME RESOLUTION OBTAINED BY A COINCIDENCE SYSTEM

In view of the importance, as discussed in Chapters 3 and 4, of a good time resolution τ when attempting to measure the frequencies ω_n of a quadrupole interaction using a coincidence system of the type mentioned in Chapters 1 and 3, we sketch in this chapter the main outlines of the factors affecting the time resolution of such a system. Complete theoretical treatments of this subject applied to systems involving scintillators and photomultiplier tubes (PMT's) are given in References (26-27).

The type of set-up that is commonly used for timing and was employed here is the "fast-slow" coincidence system and its basic components are shown in Figure 6.1. Radiation from the source interacts with the atomic electrons in the scintillator material via such processes as the Compton, photo-electric and, at high energies, pair production effects causing them to become excited. These excited electron states then decay emitting quanta of light with an emission spectrum

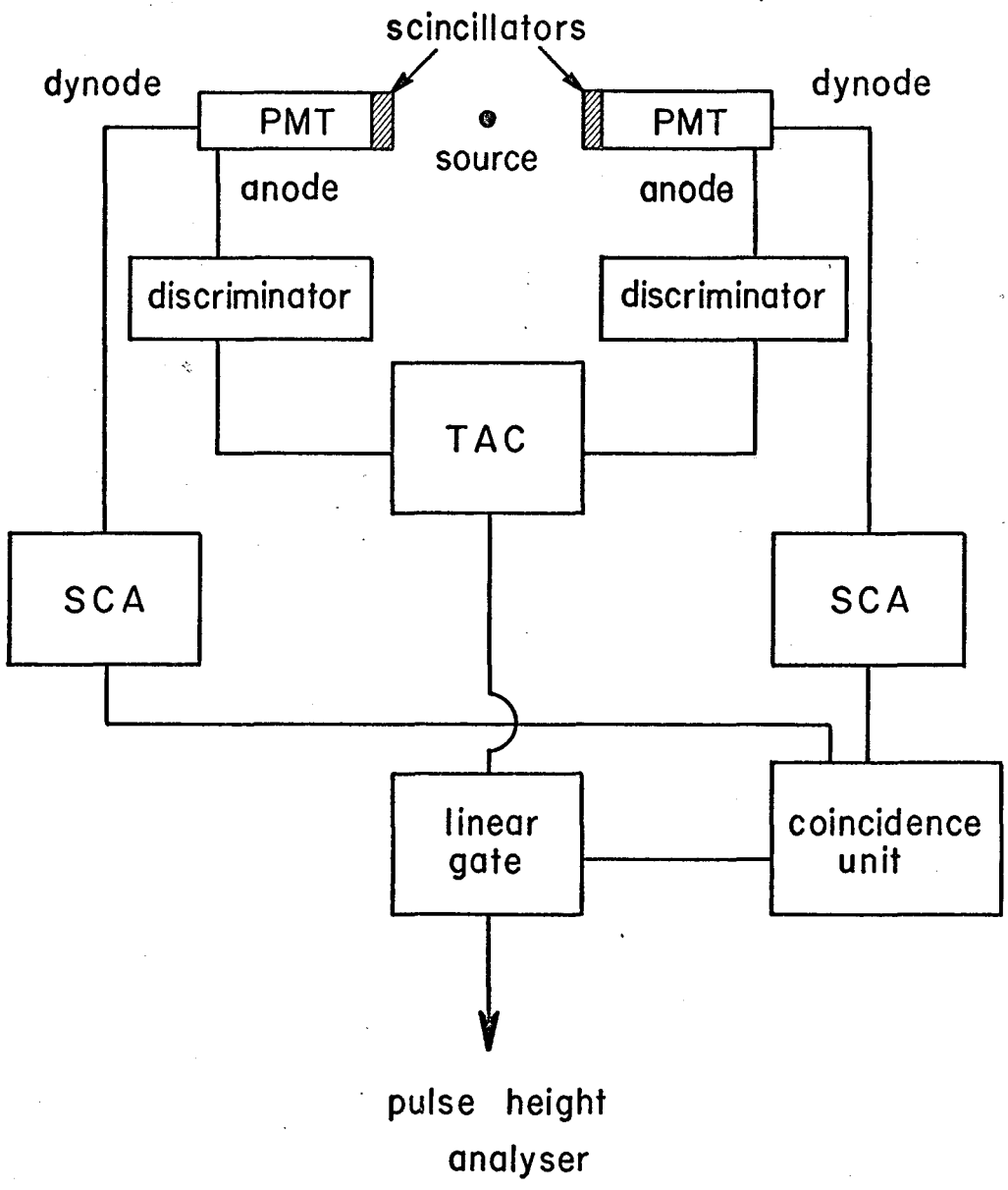

FIGURE 6·1 The basic layout of a fast-slow coincidence system.

characteristic of the scintillation material used. The intensity of the emitted light will depend on the energy of the impinging radiation. The scintillators are optically coupled via silicone grease to the faces of the PMT's, the whole assemblies being light tight to the outside. These light flashes from the scintillator cause a number of photo-electrons dependant on the intensity of the light flash and the spectral response of the tube to be emitted from the photocathode surface on the inside face of the tube. These are accelerated through a high voltage down the dynode structure causing, by avalanche processes, a large multiplication of the original number of photo-electrons. These are collected at the anode and the current thus produced is used to develop negative voltage pulses across a resistor with a height dependant on the initial energy deposited in the scintillator. The rise time of the pulse is mainly a characteristic of the tube, as the scintillator rise time is almost instantaneous, but the decay time of the anode pulse is a convolution of the tube response to a single photo-electron and the decay time of the scintillator.

These fast negative anode pulses are used for timing, in this case by the method of "leading edge triggering", i.e., they are fed after amplification to

the two discriminators which extract the timing information by triggering at variable levels on the leading edges of the anode pulses. The discriminator output pulses are then used to start and stop the TAC which gives outputs equal in number to the stop pulses falling in its time range.

Slower, integrated, pulses are taken from a suitable dynode such that their height is proportional to the energy deposited in the scintillator, and are used to extract the energy information. They are shaped and amplified before being fed into the single channel analyzers (SCA) which only give outputs for pulses falling in a certain voltage window. This can be set to correspond to gamma rays in particular energy ranges, around 133 KeV on one side, and 482 KeV on the other in our case. The outputs then go to the coincidence unit which will give outputs to gate the TAC pulses to the pulse height analyzer if the two SCA pulses arrive within the resolving time τ. This ensures that all TAC outputs other than those gated by accidental coincidences originate from pairs of gamma events from the same nucleus.

If two prompt gamma rays, such as the two 511 KeV gamma rays from the annihilation of positrons emitted by Na^{22}, are subjected to the system, a prompt time curve such as those in Figure 7.3 is obtained in the analyzer.

This corresponds to the response curve of the system for events at that energy. Its FWHM can be assigned as τ, the time resolution of the system, and its value depends on the factors described below.

6.1 THE SCINTILLATORS

The main contributions to the finite width of the prompt response curve from the scintillators come from the following two sources:

1. The variation of the time of interaction with the scintillator. This can be minimised by using an appropriate geometry and small scintillators, although the latter causes a reduction in count rate.

2. The finite decay time of light emitting states in the scintillator, and to a lesser degree the variations of times of flight of the photons to the photocathode. The decay times depend very strongly on the type of scintillator used. In our case two types are used; NaI crystals and "Naton", a kind of plastic. NaI has a decay time of 250 nsec while that of plastic is very much less about 2 nsec. This has a strong influence on the time resolution, the theory of which was originally worked out by Post and Schiff[26] who showed that the probability of arrival of the first photo-electron at the anode due to the scintillator statistics

varies as $dW = \exp(-Rt/T)dt$ where R is the number of photoelectrons produced at the cathode by a photon of energy E and T is the decay time of the scintillator response to a single photon. T/R is then the width of the exponential.

If this width is not negligible compared to that of the response of the tube to a single photoelectron produced at the cathode, the time resolution is limited by the scintillator statistics and the discriminator is set to trigger on the first photoelectron, as distinguished from the inherent noise of the tube. This is the case with NaI at low energies, and hence small R, because of the long decay time. At higher energies, and larger R, the slope of the prompt curve due to the NaI statistics varies as 1/E up to a certain limit.

This is not the case with plastic as its decay time is so short the decay of the anode pulse is essentially that of the SER of the tube. In this case, Gatti and Svelto[27] show that the best time resolution is obtained when the discriminator is set to trigger at a significant proportion of the total pulse amplitude. Usually for plastic the trigger level is set to correspond to 10 per cent of the height of the Compton continuum to be described later in this chapter. At high energies

significantly shorter time resolutions can be achieved with plastic than with NaI, for instance, for the two prompt 511 KeV gamma rays a typically attained figure for τ with two plastic scintillators is 0.36 nsec; and 0.80 nsec for NaI. The actual values achieved can be a little more or less, according to the stability of the system and the noise of the tubes being used; but the best values are always higher than the theoretical limits. The reasons for this are not yet entirely understood. The minimum time resolution is energy dependant and is shown by Gatti and Svelto to vary as $(E)^{-1/2}$, where E is the energy lost in the scintillator; but experiments show that this is only true for energies below about 2 MeV and reaches a limit for higher energies.

Plastic has a lower Z than NaI and hence a lower efficiency at the same gamma ray energy, which means that the response of plastic to a monoenergetic gamma ray is almost entirely due to the Compton process and is a continuum with no photopeak, while that of NaI contains a definite photopeak whose centroid corresponds to the energy of the gamma ray. Thus the energy deposited by a photon of energy E in plastic is always less than that deposited in NaI. At low energies, therefore, the timing advantage of plastic over NaI is reduced as the latter remains limited by statistics. Also different gamma

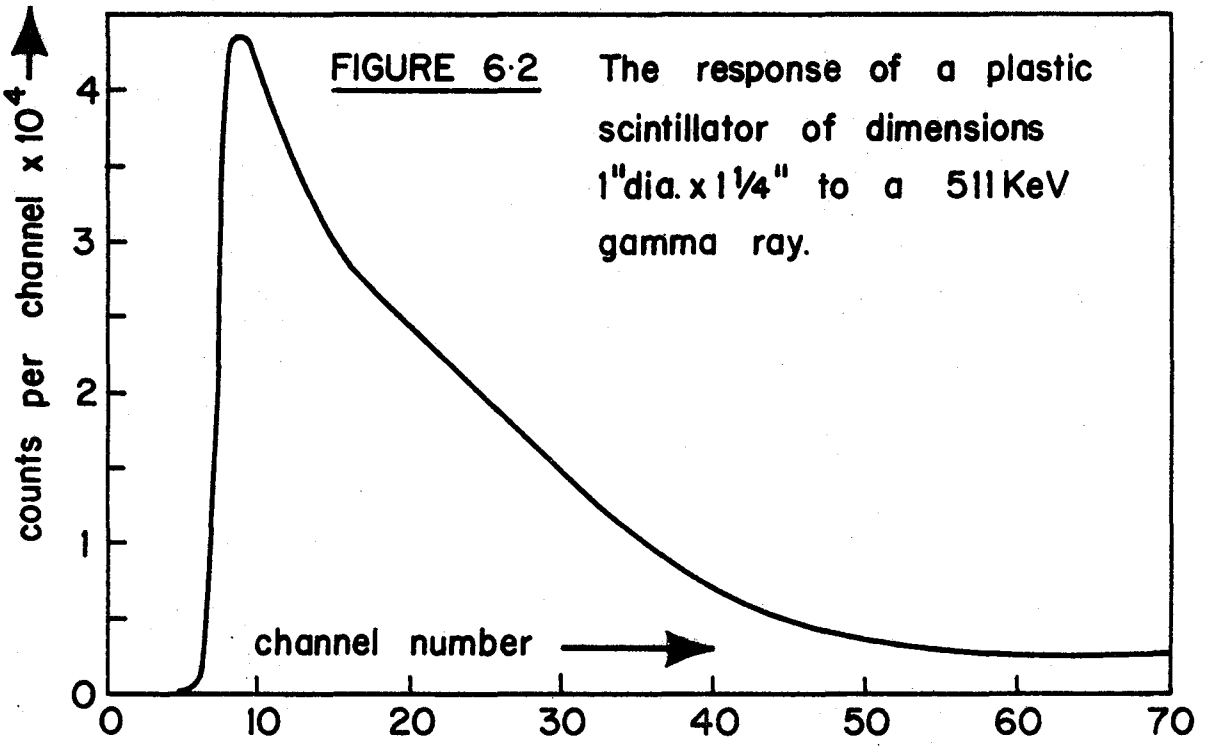

FIGURE 6·2 The response of a plastic scintillator of dimensions 1"dia. x 1¼" to a 511 KeV gamma ray.

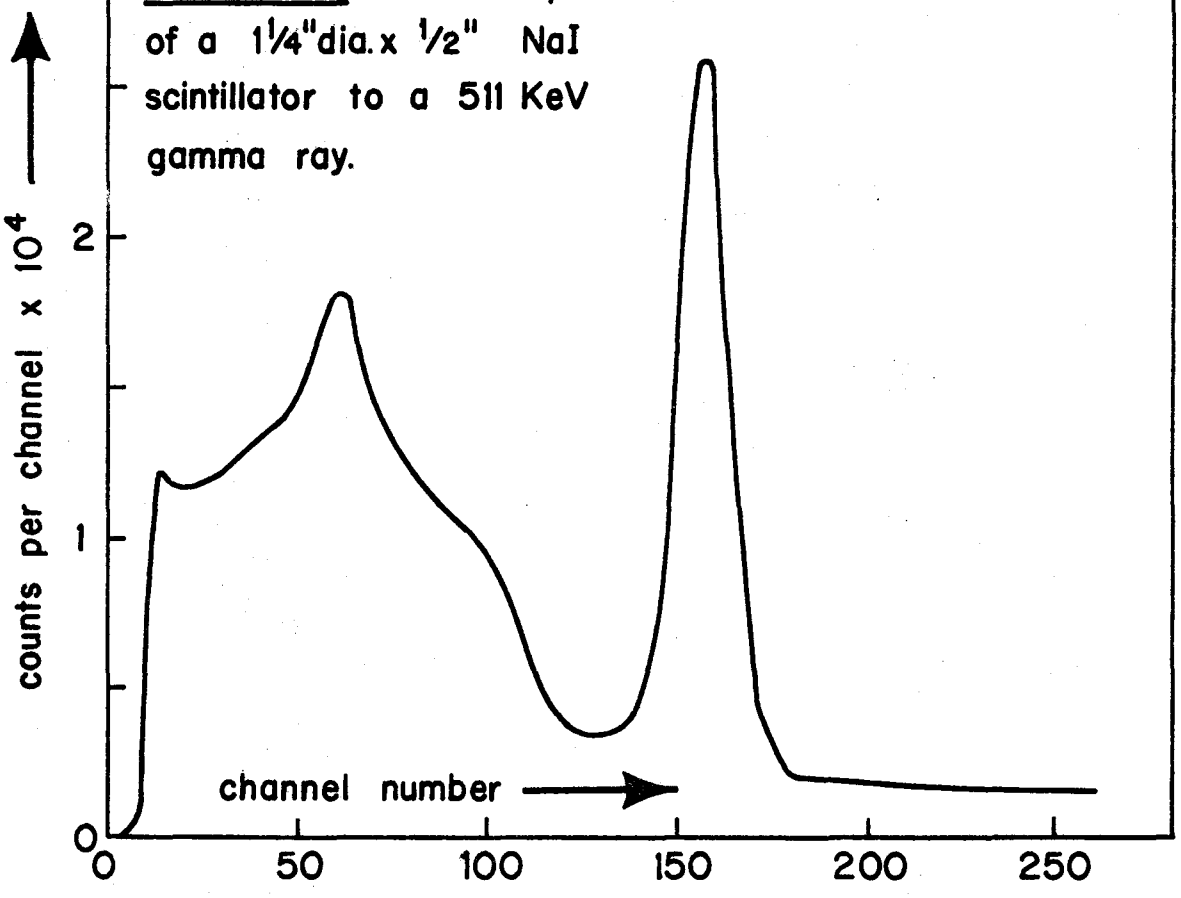

FIGURE 6·3 The response of a 1¼"dia. x ½" NaI scintillator to a 511 KeV gamma ray.

rays can be resolved using NaI, if their separation is outside the energy resolution, by setting the SCA windows on the photopeaks; but this is not so easy with plastic. For example, Figure 6.2 shows the response of plastic to the 511 KeV gamma ray from Na^{22}, and Figure 6.3 shows that of NaI to the same gamma ray.

6.2 THE PHOTOMULTIPLIER TUBES

Here the main effects contributing to the time resolution from the PMT's are:

1. Variation of transit time of the photo-electrons and secondary electrons due to different path lengths, and variation of initial angle and energy of the secondary electrons. This is minimized by tube design.

2. The finite rise time of the anode pulse. This must be as short as possible when using plastic to minimize the variation of triggering time with pulse height (or "walk"). This increases with decreasing slope as shown in Figure 6.4. To reduce the time walk some energy restrictions must be imposed. With NaI the SCA's are set on the photopeak of the gamma ray of interest, while in plastic it is usual to set the SCA window on the upper 20 per cent of the Compton edge. The fastest tube available today, the RCA 8575, has an anode rise time of under 2 nsec.

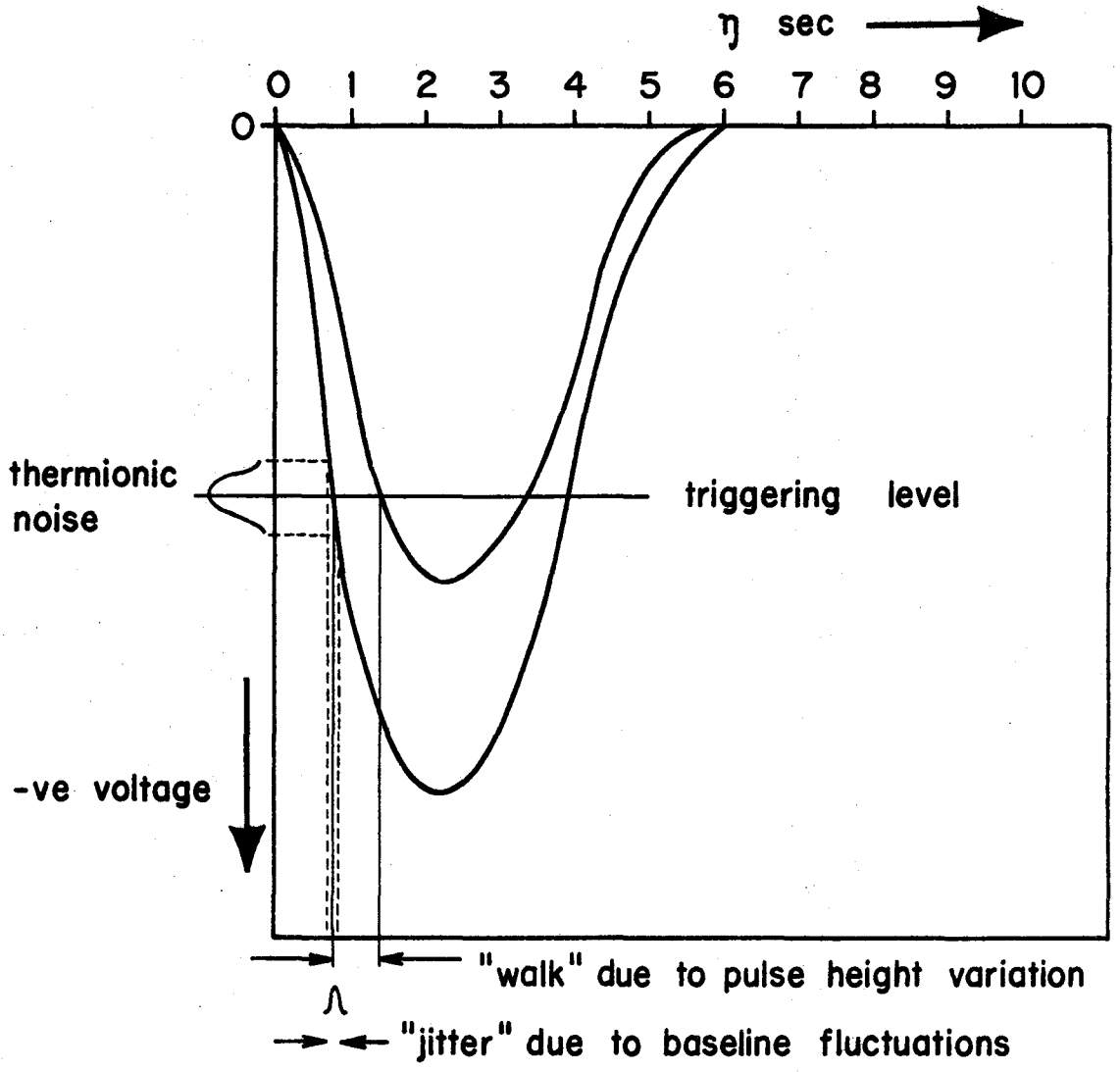

FIGURE 6·4 Effect of anode pulse height variation and noise on timing with plastic.

3. The rms noise originating from thermionic electrons. The effect of this on the time resolution can be seen by referring to Figure 6.4. Statistical fluctuations of the baseline due to noise will be superimposed on the anode response with time and will cause variations in the triggering level, and hence the triggering times. It can be appreciated that the effects due to noise are minimized by having as short a rise time as possible, and the best tubes for timing, such as the RCA 8575, combine low noise with fast anode rise time. The characteristics of a PMT are determined by its single electron response which is the response of a PMT to a single photo-electron.

6.3 THE ELECTRONICS

The main factors concerning the associated electronics that affect the time resolution are jitter and long term drifts. The jitter will come mainly from small variations in the discriminator triggering levels which can only be dealt with by careful design. It can be measured by triggering both discriminators of fast-slow coincidence system with the same anode pulses, when it is usually found to be very small, less than 0.1 nsec.

Drifts are more serious in long experiments and can be caused by temperature variations or mechanical vibrations over long periods.

CHAPTER 7

THE APPARATUS AND EXPERIMENTAL PROCEDURE USED IN THE INVESTIGATION OF THE QUADRUPOLE INTERACTION OF Ta^{181} IN HAFNIUM OXIDE

Four sets of runs were made during the study of the perturbation of the angular correlation of the 133-482 KeV cascade in Ta^{181} by the interaction of its quadrupole moment with the electric field gradients in a HfO_2 polycrystalline environment. Variations in the conditions were made in each set of runs: of the detectors in the first three cases in attempts to improve the time resolution, and in the fourth the HfO_2 was annealed to reduce any lattice defects due to irradition.

7.1 THE DETECTORS

The combinations of scintillator and PMT used in the four sets of runs were as follows:

Runs (1): Two NaI scintillators mounted on RCA 8575 PMT's were used at first in order to utilize the

high efficiency of NaI and gain in count rate, and hence statistics. The 133 KeV gamma rays were detected in a 1" x 1/2" crystal and the 482 KeV in a 2" x 1" crystal. SCA windows were set on the photopeaks in each case. High chain current (12 ma at 3 KV) bases were used to supply the dynode voltages as the long decay of the NaI anode pulses produce large quantities of charge at the anode. If the anode current becomes significantly large compared to the chain current the dynode voltages are affected and a gain shift with rate occurs. The time resolution for 133-482 KeV, as shown in Figure 7.3, was inadequate to resolve the higher frequencies when the data was analyzed so certain changes were made in Runs (2).

Runs (2): In this case, in order to improve the time resolution, the NaI scintillator on the 482 KeV side was replaced by a 1" x 1-1/4" plastic one. The RCA 8575 tube on this side was replaced by a RCA 6810 which has a slightly slower rise time and higher noise, but was included at this stage to test its capabilities as it was hoped to include it in a three counter experiment later on. Due to the availability of equipment at this time the high current base on the other side had to be changed to a low current (2ma at 3KV) Ortec base, so some gain shift with rate had to be reckoned with as the Hf^{181} beta

decayed to Ta^{181} with its 40 day half-life. However, the anode current of this base was reduced by shielding the detector with a thin sheet of cadmium which completely absorbed the 50 KeV gamma ray, but allowed the 133 KeV through with only about 10 per cent attenuation. A 1/8" thick lead shield over the plastic scintillator eliminated the 133 KeV gamma rays from that side leaving just the 482 KeV. Energy selection was then made by setting SCA windows on the 133 KeV photopeak in the NaI and on the upper 20 per cent of the Compton continuum in the plastic. The time resolution, as shown in Figure 7.3, was still not satisfactory at 2.4 nsec., so further changes were made for runs (3).

Runs (3): The scintillators in this case were as for runs (2) but the RCA 6810 was replaced by an 8575 again and a high current base restored to the NaI side. A prompt component was observed to be present in the decay curve of the 482 KeV level, which was assumed to be due to Compton photons, being backscattered from one scintillator to the other. Lead shielding in the 45 degree position between the counters greatly reduced this prompt contribution. This set-up achieved the best time resolution of 1.3 nsec.

Runs (4): The detectors were as for runs (3) but measurements were made on an annealed source as described in Section 3.

7.2 THE ELECTRONICS

The block diagram of the electronic system as used in runs (3) and (4) is given in Figure 7.1. The set-ups in the other sets of runs were basically very similar. The long NaI anode pulses tend to cause trouble in the discrimination as the discriminator will double pulse on the long tail of the anode pulse, which also sometimes has some positive overshoot. The Ortec 417 discriminator is specially designed to handle such anode pulses and features an internal stretcher. An amplification of the NaI anode pulses by 100 times was necessary in order to trigger near the noise levels, as the 417 discriminator has a minimum triggering level of 150 mV. The limiter inserted between the two stages of amplification eliminated the positive overshoot.

The SCA outputs fire on the cross-overs of the bi-polar outputs of the two double delay line amplifiers. On the plastic side the cross-over time comes before that of the NaI, so in order to get the SCA outputs in time at the coincidence box a 0.5 μsec delay was inserted in the plastic side.

Although the 133 KeV gamma ray is emitted from a Ta^{181} nucleus before the 482 KeV the latter were used to start the TAC. This is because the NaI has a higher

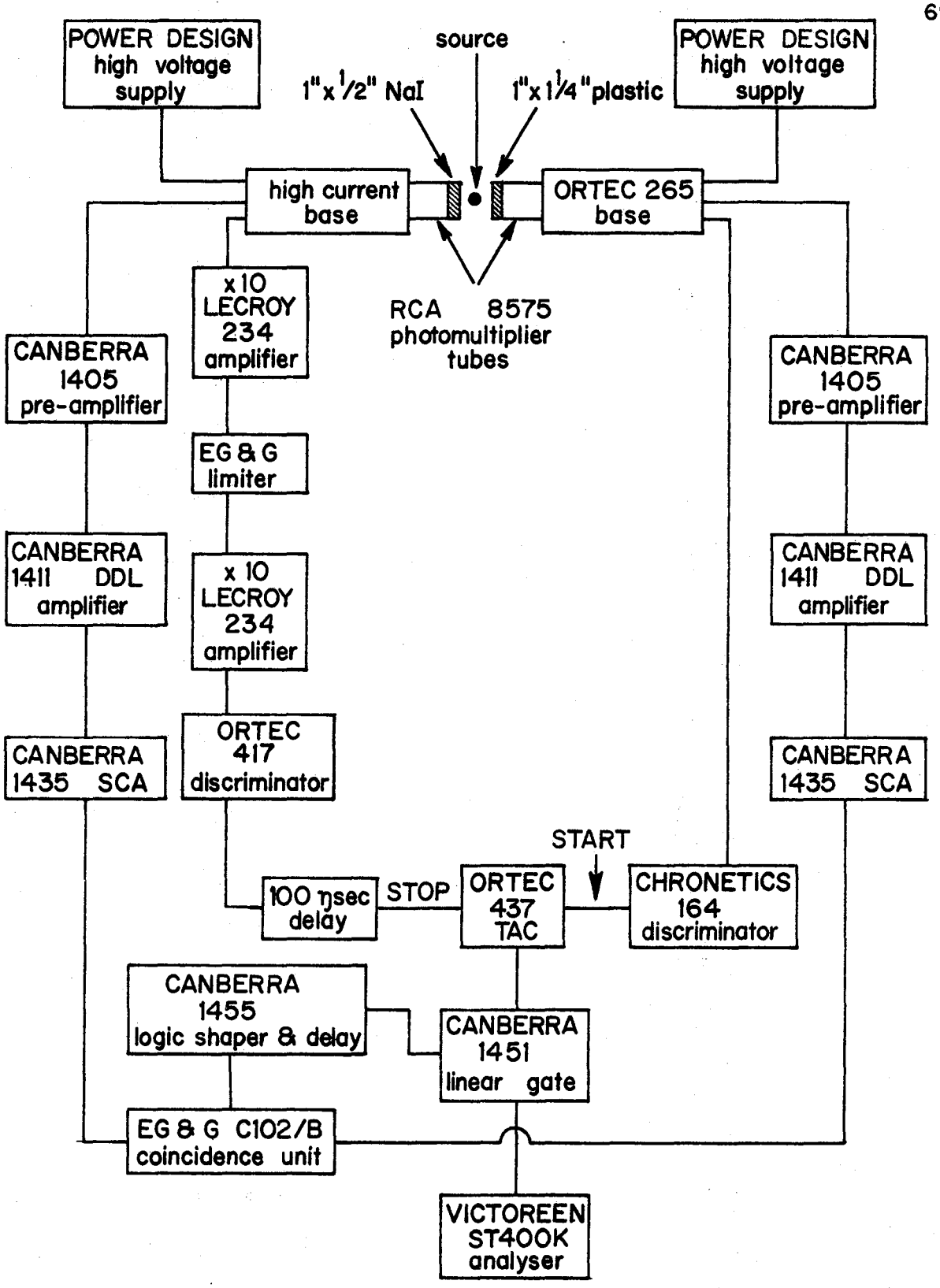

FIGURE 7·1 The electronic system.

efficiency than plastic and, as the TAC rate is governed by the stop rate, this arrangement allows a higher TAC count rate. The decay curve of the 482 KeV level is then obtained in the analyzer "back to front".

7.3 THE SOURCE

The HfO_2 powder was supplied by Johnson Matthey and Co. Ltd. and was specified as being of spectroscopic purity. Fifteen mgms were irradiated in the McMaster University Nuclear Reactor Irradiation Facility for 8 MWH's in the first instance and received further irradiations of 8 and 10 MWH's to restore the source strength. A singles gamma spectrum was taken after the second irradiation with a Ge(Li) detector and is shown in Figure 7.2 with the main peaks identified. The large peak at about 1 MeV was due to the activation of zinc present in some Scotch-Tape that was around the sealed quartz capsule containing the HfO_2 during the irradiation.

In order to reduce the effects of nuclear recoil following irradiation the source was annealed for runs (4) by heating it to 1200 K for four hours and slowly cooling it over eight hours. The effects of this are discussed in Chapter 9.

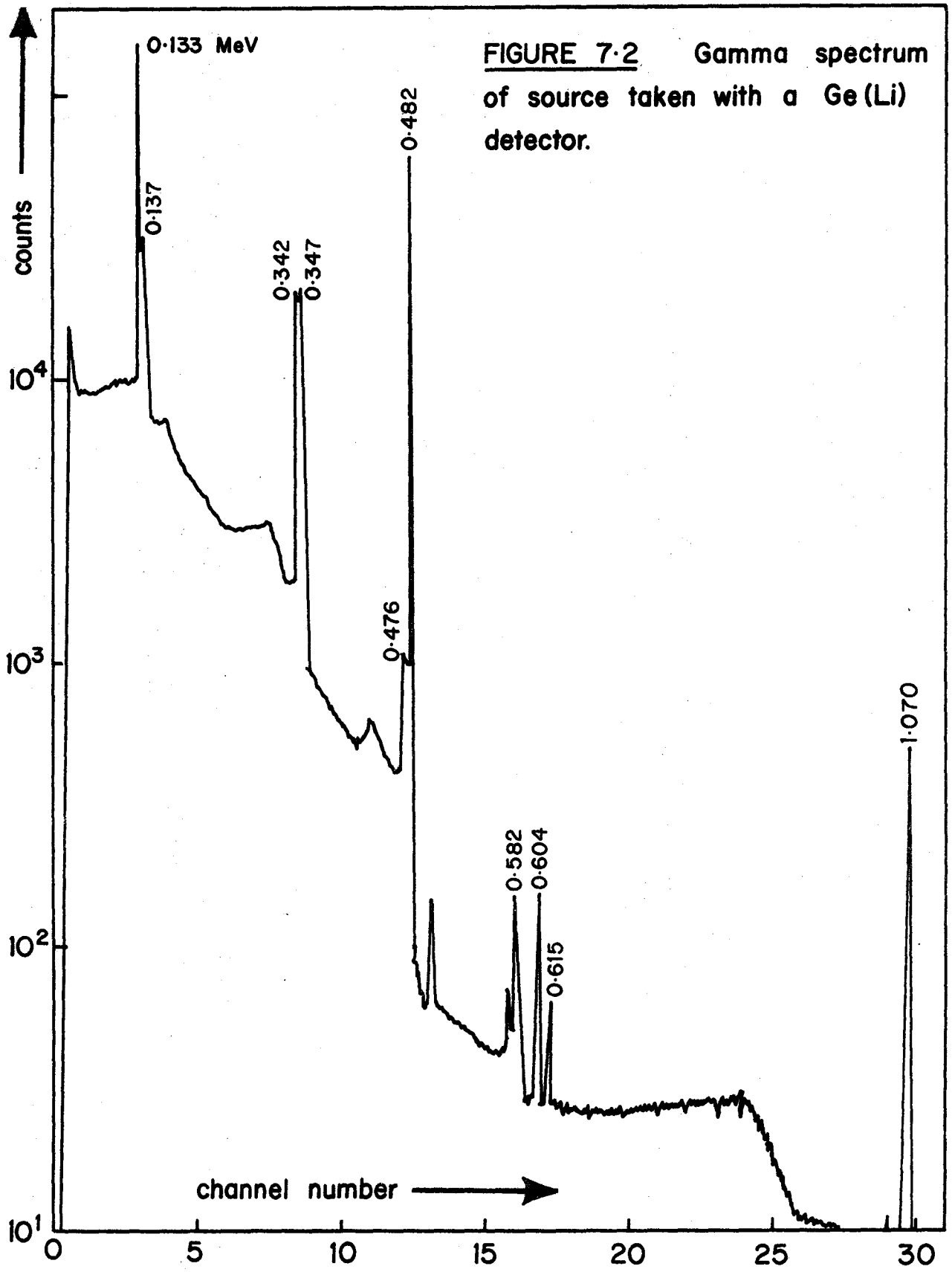

FIGURE 7·2 Gamma spectrum of source taken with a Ge(Li) detector.

7.4 THE MEASUREMENT OF THE TIME RESOLUTION

In order to obtain the time resolution of the system shown in Figure 7.1 for coincidence between 133 and 482 KeV gamma rays, the groups of two prompt 511 KeV gamma rays resulting from the annihilation of positrons emitted by the beta decay of Na^{22} were subjected to the two counters which subtended an angle of 180 degrees, the angle of emmission of the two prompt gamma rays.

The plastic sides were set as for the 482 KeV gamma ray. The SCA window on the NaI side was set on the 511 KeV photopeak, the linear amplifier gain was then turned up by a factor of four to accept an energy of approximately 130 KeV. The prompt curves thus obtained for the runs are shown in Figure 7.3 where the improvement in time resolution from runs (1) to (4) is clearly shown. The gaussian shape of the curve is displayed by the slopes which, on the logarithmic plots, are straight lines.

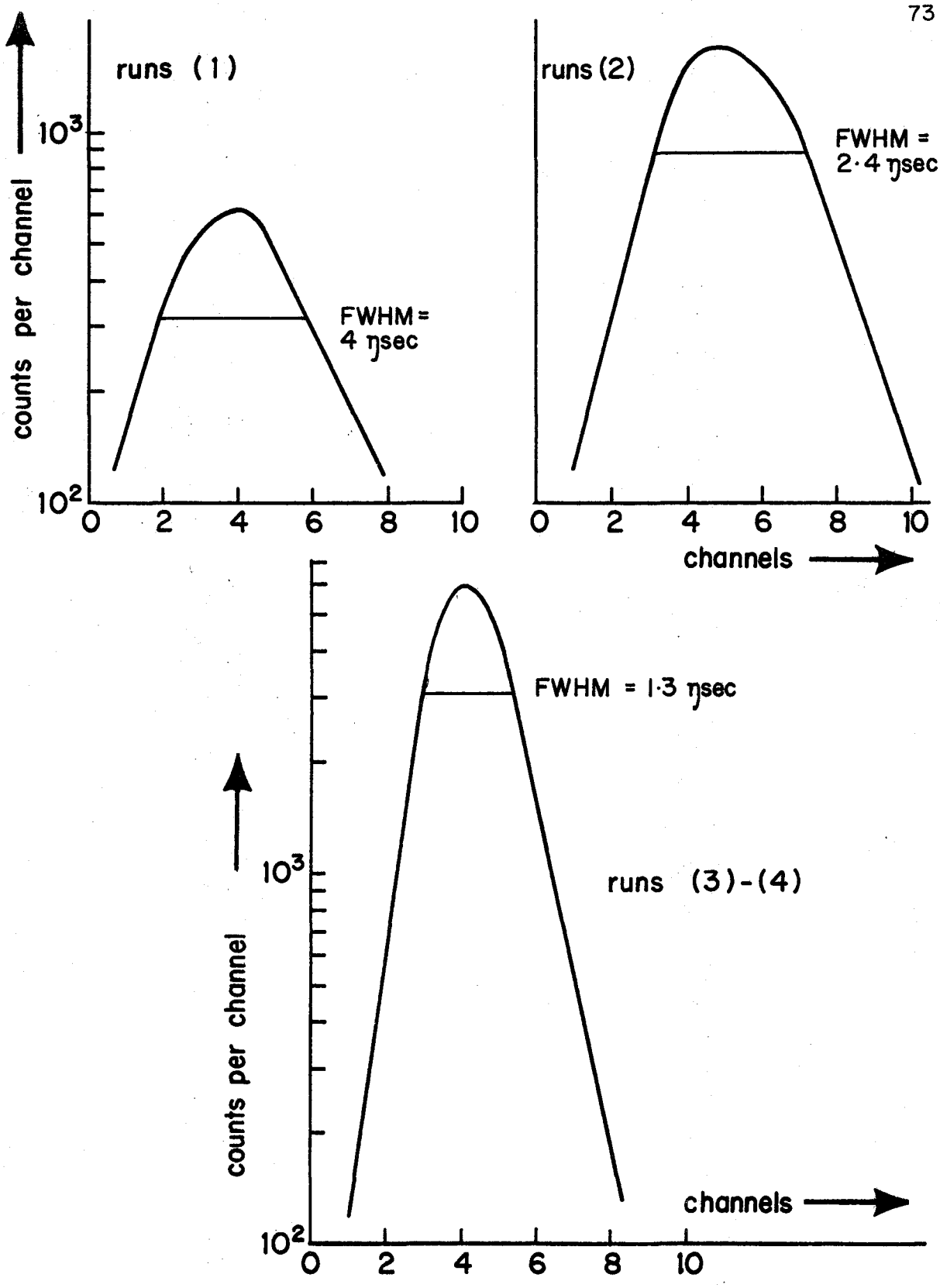

FIGURE 7·3 The prompt curves used in runs (1) - (4).

7.5 THE PROCEDURE FOR THE PAC MEASUREMENTS

The decay curves of the 482 KeV level of Ta^{181} were taken with the detectors alternately subtending angles of 180 and 90 degrees at the source. The two available 90 degree positions were alternately used in order to eliminate errors due to source centering. Counting was done for 24 hours at each angle collecting about 10^4 coincidences according to source strength. The information stored in the analyzer was recorded at the end of each counting period. In runs (1) all the time spectra for 180 and 90 degrees were totalized and analyzed by the Fourier transform method described in Chapter 4. In runs (2) several smaller batches of 180 and 90 degree runs were added up while in runs (3) and (4) individual pairs of runs were analyzed.

In order to monitor drifts in the tube gain the SCA window on the NaI side was scaled every 24 hours and checked against the decay of the source. Discriminator drifts were checked by scaling the discriminator outputs. If serious drifts occurred adjustments were made to restore the system to order. It was found that drifts were minimized and reliability improved by proper temperature control. The laboratory was air-conditioned with a temperature of 70 degrees fahrenheit maintained

in the room. The cabinet containing the electronic modules contained forced-air cooling.

Examples of the time spectra $W(\theta,t)$, $E(t)$, $G_{22}(t)$ and the Fourier power spectra obtained from them are shown in the next chapter.

7.6 THE TIME SCALE CALIBRATION

In order to obtain a time scale calibration for the time spectra stored in the analyzer a special calibrator developed by Boulter et al[28] was employed. This consists of an rf oscillator, the signal from which correlates the start and stop pulses to the TAC in such a way that the start-stop time is restricted to a random multiple of the rf oscillator period. The resulting peaks that are generated across the TAC time scale are separated by one oscillator period and yield the time scale calibration. An example of the calibration spectrum is given in Figure 7.4.

The linearity of the system was also obtained from the time scale calibration by calculating the centroid positions of the calibration peaks to a fraction of a channel and examining the separations of the peaks as a function of channel number. This revealed that the first 220 of the 400 channels exhibited no significant

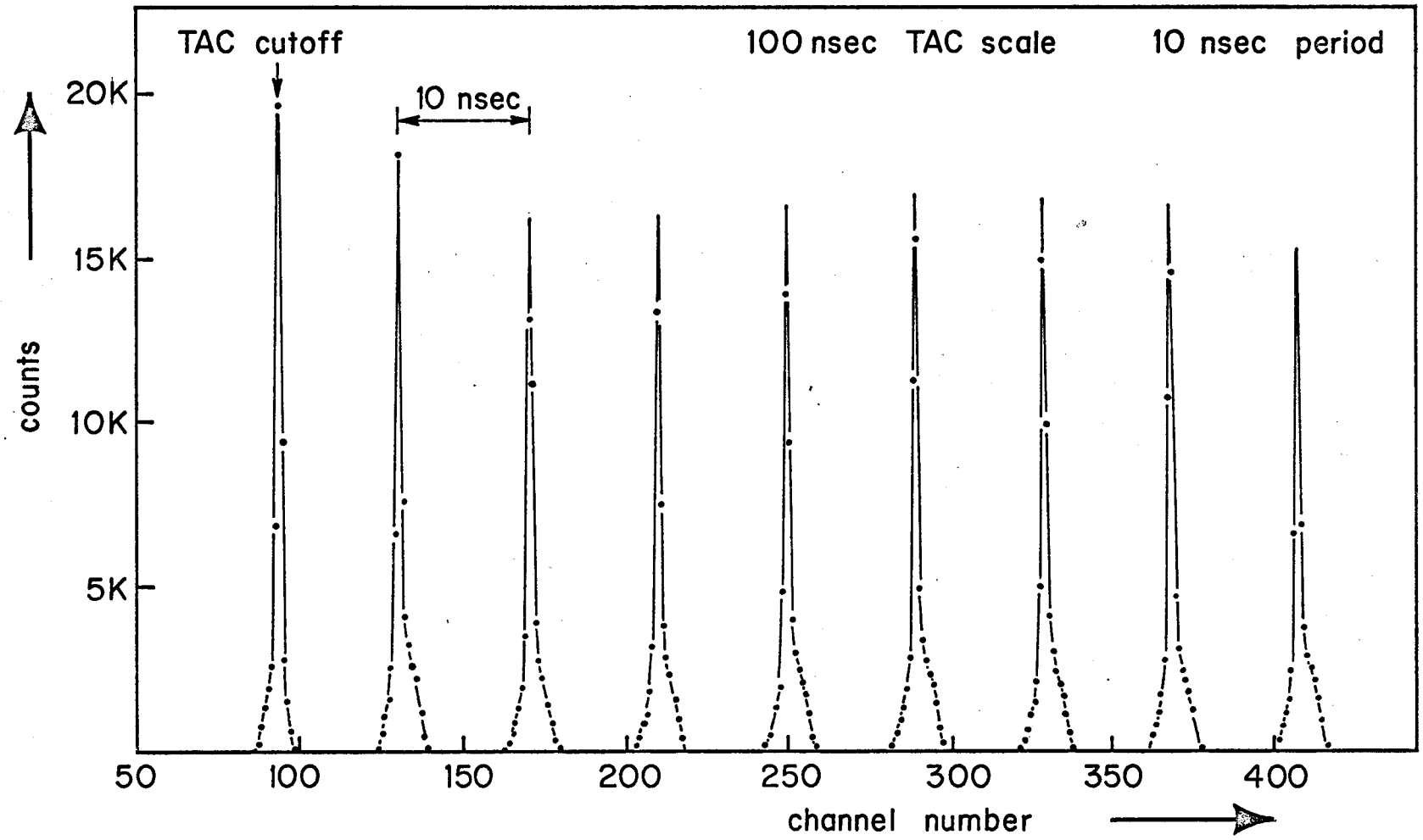

FIGURE 7·4 The calibration peaks obtained from the TAC timescale calibrator.

departures from linearity and with the TAC time scale being used represented a timescale calibration of .536 nsec/ch. However, the remaining 180 channels exhibited a non-linearity which tended to reduce the peak separation with increasing channel number. The mean calibration in the last 20 channels was 0.592 nsec/ch., representing a maximum departure from linearity of about 10 per cent. The analyzed data was extracted from channels in the region of number 230 to 320 and over this region the mean time scale calibration varied from 0.559 to 0.551 nsec/ch. according to the actual region used. The effect of the non-linearity of the time scale over this region on the Fourier spectrum of the $G_{22}(t)$ function has not been fully investigated at present.

7.7 A CHECK ON THE STABILITY OF THE SYSTEM BY A CENTROID SHIFT METHOD

A check was made on the stability of the electronics and the time scale calibration by measuring the shift in the centroid of the prompt time curves obtained from two prompt 511 KeV gamma rays with a known delay inserted in the stop side of the fast coincidence system.

This was done by mounting the source on an optical bench saddle equipped with a micrometer screw type arrangement that allowed small displacements to be made along

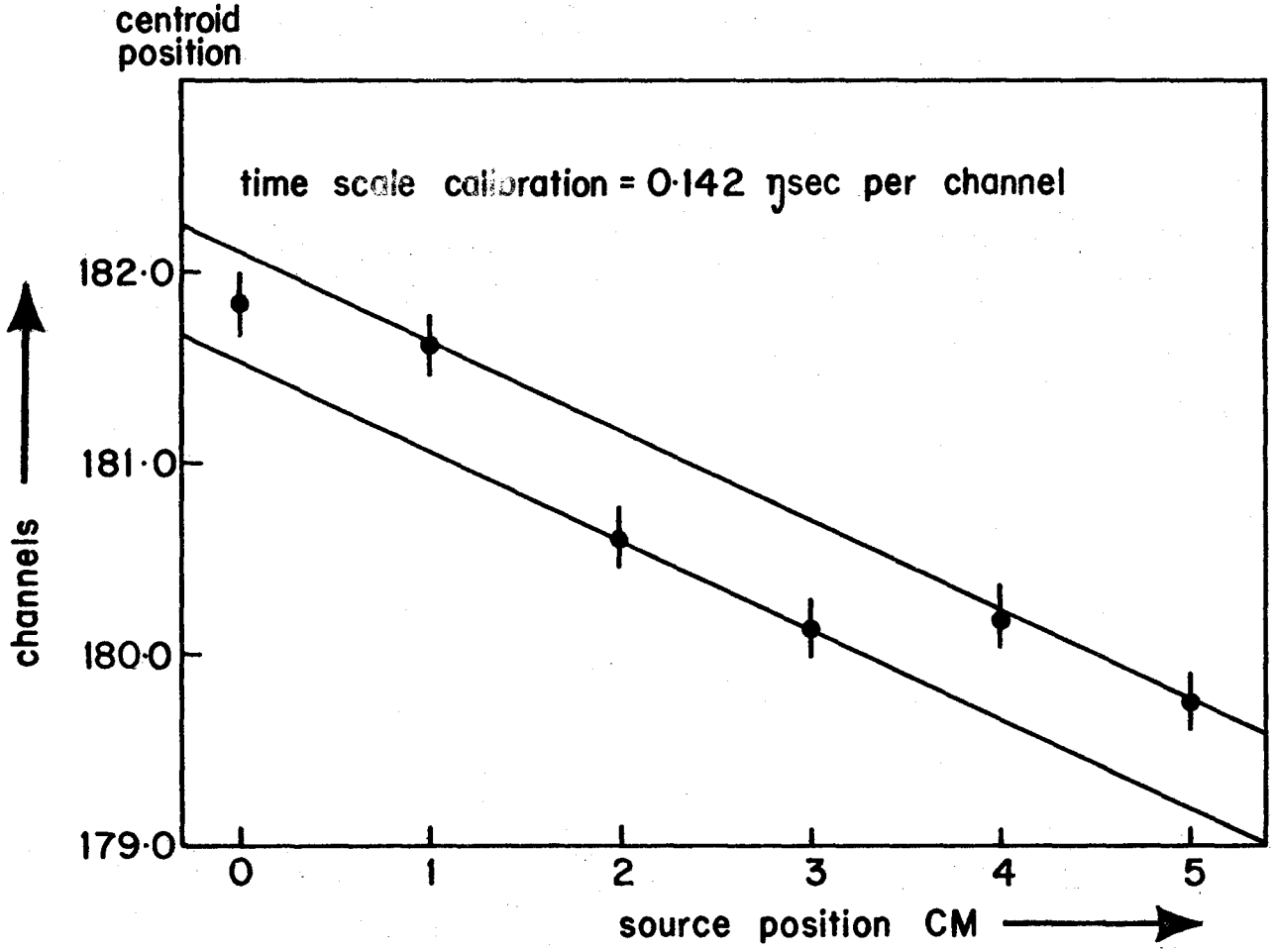

FIGURE 7·5 The variation of prompt centroid with source position.

the axis of the detectors which subtended an angle of 180 degrees at the source. The delay was then due to the finite velocity of light as the source was moved away from the stop detector, and was equal to twice the time taken for light to traverse the distance of displacement.

In Figure 7.5 the position of the prompt centroid is plotted against source position, when it can be seen that within the statistics of the numbers involved the centroid position is a linear function of the delay. The slope of the line joining the data points is twice the reciprocal of the velocity of light which, from the graph, is shown to be 30 cm per ns., which is a reasonable value for c. This indicates the time scale to be a valid one and the system is linear over a small channel range. There is, however, a basic time uncertainty due to instabilities which, from the spread of the data points, can be assigned as about 0.085 nsec.

CHAPTER 8

THE RESULTS

8.1 THE ANALYSIS OF THE DATA

The decay curves W(180,t) and W(90,t) obtained from runs (1), (2), (3) and (4) were analyzed in different ways as follows:

Runs (1): Here the individual 180 and 90 degree time curves were totalized and the Fourier power spectrum obtained from the ratio of the totalized runs after subtraction of the chance backgrounds and the constant component in the ratio. However, as mentioned in the last chapter, the time resolution was inadequate to resolve any frequencies higher than ω_0 and so these runs were discarded.

Runs (2): In order to minimize the effects of zero time point shifts in the time curves caused by the gain shifts with rate discussed in the previous chapter, four smaller batches of runs were totalized and analyzed. This time the time resolution enabled good measurements of ω_0 and ω_1 to be made but ω_2 remained unresolved.

Runs (3): In this case six individual pairs of runs were analyzed as the increased source strength allowed sufficiently good statistics to be obtained in a 24 hour period. The improved time resolution meant that in these runs all three frequencies could be resolved.

Runs (4): Four pairs of individual runs were analyzed and values of ω_0, ω_1, and ω_2 obtained. Examples of W(180,t), W(90,t), the ratio E(t) and the power spectrum obtained from them are shown in Figures 8.1, 8.2, 8.3 and 8.4 respectively.

8.2 THE FREQUENCIES ω_n

The frequencies obtained from all the above runs after corrections to the zero points described in Section 8.7 were applied, are tabulated in Table 8.1. From these values the means of ω_0, ω_1 and ω_2 were calculated and are given in Table 8.2. When a mean from a large population is obtained the error is estimated by the standard deviation σ or the root-mean-square deviation from the mean, but the population from which the mean frequencies are taken is too small for this to be a reliable estimate of the error; it would, in fact, be an under-estimate.

In such cases confidence intervals for population means and the "Student t" distribution are used. A

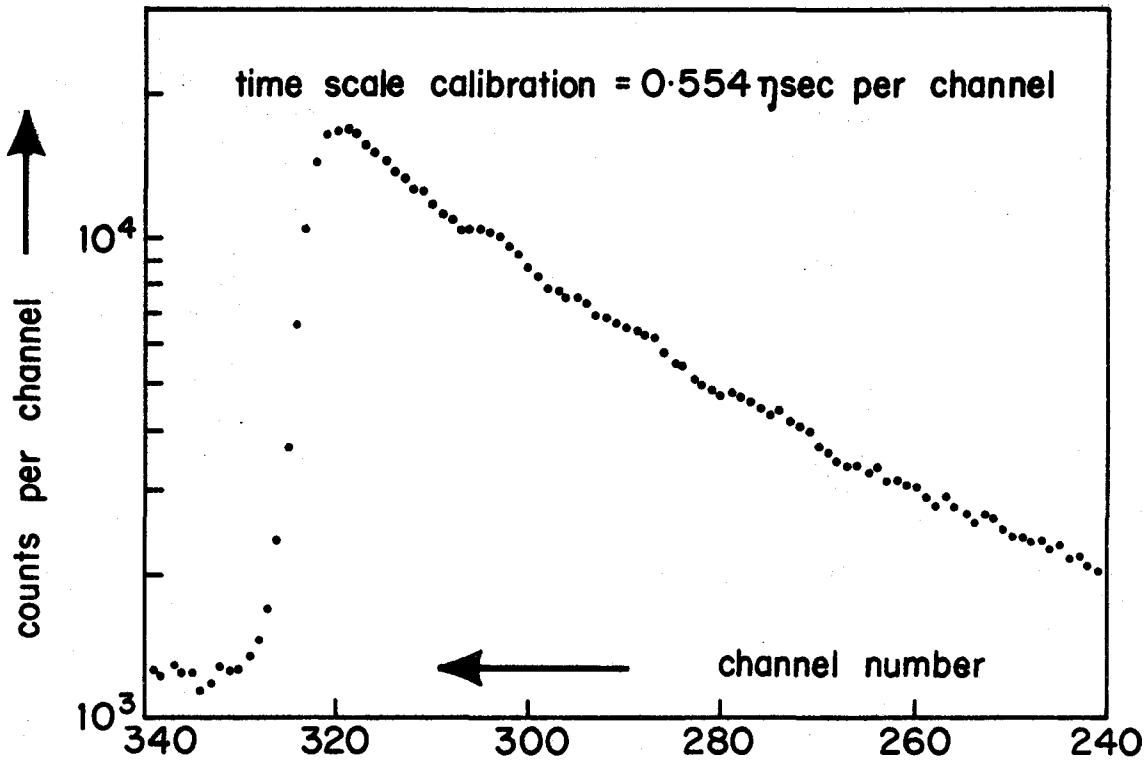

FIGURE 8·1 An example of a 180 degree decay curve.

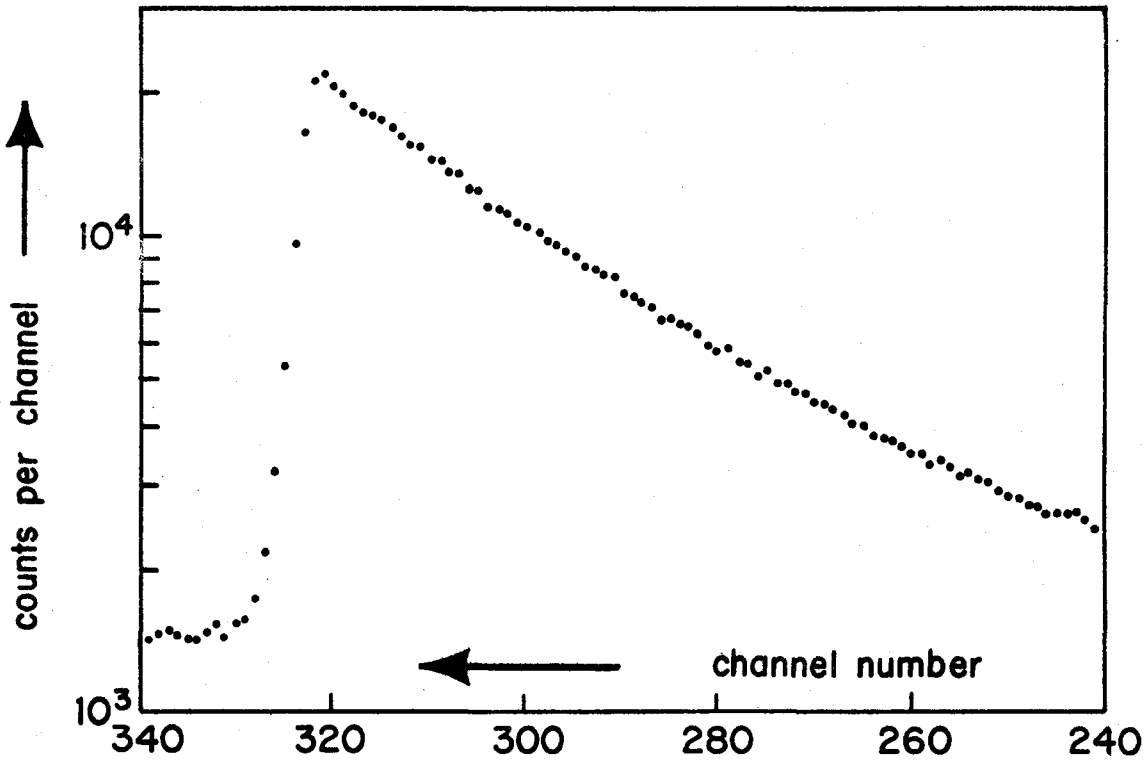

FIGURE 8·2 An example of a 90 degree decay curve.

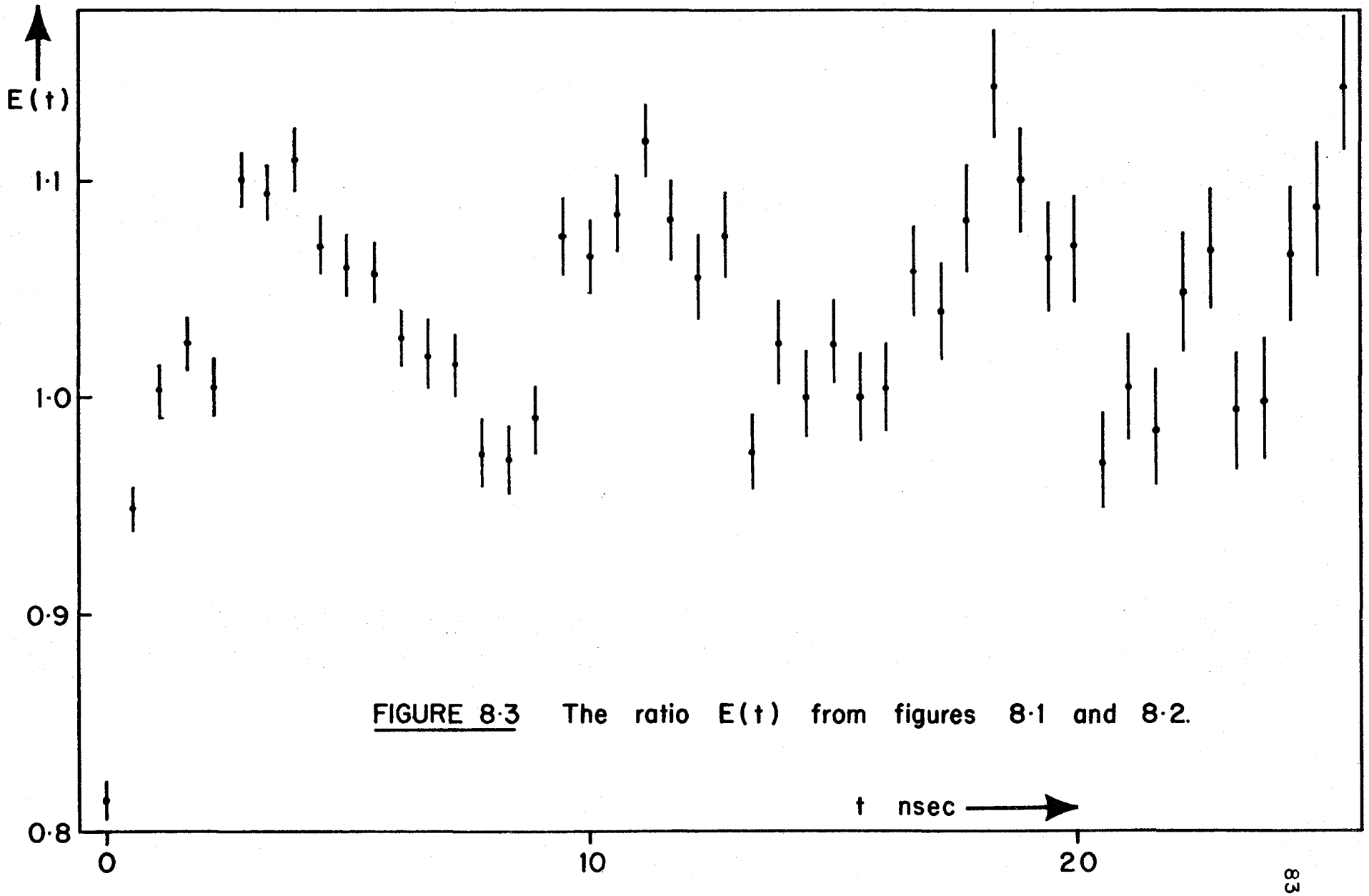

FIGURE 8·3 The ratio E(t) from figures 8·1 and 8·2.

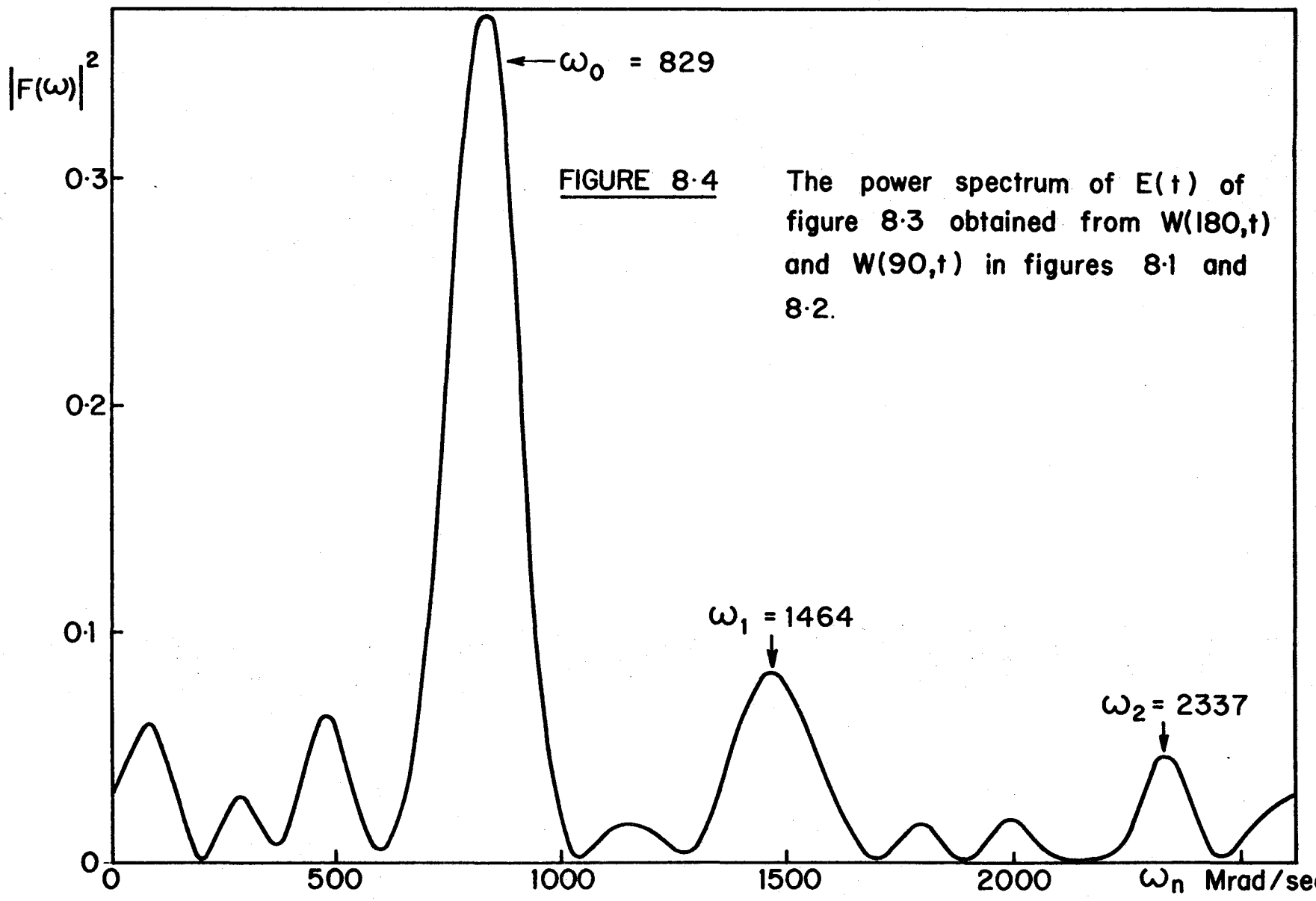

FIGURE 8·4 The power spectrum of E(t) of figure 8·3 obtained from W(180,t) and W(90,t) in figures 8·1 and 8·2.

confidence interval for the mean, μ of a population is an interval for which one can assert with a given probability that it contains μ. If the sample size, n, is small and the variance, σ^2, unknown, the t distribution is used to obtain confidence intervals for μ.

If we have n data points x_i, where i runs from 1 to n, then we can make the following definitions:

$$\text{Sample mean:} \qquad \bar{x} = \frac{\sum_{i=1}^{n} x_i}{n}$$

$$\text{Sample variance:} \qquad s^2 = \frac{n\sum_{i=1}^{n} x_i^2 - \left(\sum_{i=1}^{n} x_i\right)^2}{n(n-1)} \qquad 8.1$$

Small sample $1-\alpha$ confidence interval for μ:

$$\bar{x} - t_{\alpha/2}\frac{s}{\sqrt{n}} < \mu < \bar{x} + t_{\alpha/2}\frac{s}{\sqrt{n}}$$

where $t_{\alpha/2}$ can be obtained from statistical tables. The confidence interval for the means of the frequencies in Table 8.1 was taken as 95%. From the Equations 8.1 one can estimate the deviation from the mean of a assembly of data points, and this is done in Table 8.2 for the frequencies obtained from runs (2), (3) and (4). The frequencies in runs (4) corresponding to the annealed source can be seen not to differ significantly from those

TABLE 8.1

THE FREQUENCIES ω_0, ω_1 AND ω_2 OBTAINED FROM RUNS (2)-(4)

	ω_0	ω_1	ω_2 Mrad/sec
Runs (2):	842	1527	-
	811	1508	-
	823	1502	-
	817	1439	-
Runs (3):	804	1483	2306
	829	1470	2268
	804	1521	-
	798	1489	2425
	823	1439	2300
	829	1502	2325
Runs (4):	811	1458	2381
	823	1521	2325
	829	1464	2337
	829	1495	2425

TABLE 8.2

THE MEAN FREQUENCIES OBTAINED FROM RUNS (2)-(4)

Runs (2):	ω_0	=	823 ± 21	Mrad/sec
	ω_1		1495 ± 61	Mrad/sec
Runs (3):	ω_0	=	815 ± 15	Mrad/sec
	ω_1		1483 ± 28	Mrad/sec
	ω_2		2325 ± 67	Mrad/sec
Runs (4):	ω_0	=	823 ± 17	Mrad/sec
	ω_1		1483 ± 46	Mrad/sec
	ω_2		2369 ± 73	Mrad/sec

TABLE 8.3

THE WEIGHTED MEANS OF THE FREQUENCIES IN TABLE 8.2

ω_0	=	819 ± 10	Mrad/sec
ω_1		1483 ± 25	Mrad/sec
ω_2		2350 ± 50	Mrad/sec

from the unannealed source and so were grouped with them in the calculation of the final weighted means.

From the means and variances contained in Table 8.2 the "weighted means" $\bar{\omega}_n$ were calculated where:

$$\bar{\omega}_n = \frac{\sum_{i=1}^{n} \frac{1}{\sigma_i^2} \omega_i}{\sum_{i=1}^{n} \frac{1}{\sigma_i^2}} \qquad 8.2$$

The variance of the weighted mean is given by:

$$\frac{1}{\sigma 2} = \sum_{i=1}^{n} \frac{1}{\sigma_i^2} \qquad 8.3$$

The weighted means and their standard deviations are given in Table 8.3. The obtained frequencies can be seen to be reasonable because within the experimental limits $\omega_2 = \omega_1 + \omega_0$, as demanded by the transitions shown in Figure 2.2.

8.3 THE FREQUENCY RATIOS

The frequency ratios ω_1/ω_0 and ω_2/ω_0 obtained from the mean frequencies tabulated in Table 8.2 for the separate sets of runs are set out in Table 8.4. The standard deviations for these ratios were estimated as

TABLE 8.4

THE FREQUENCY RATIOS CALCULATED FROM TABLES 8.1 AND 8.2

Runs (2)	$\omega_1/\omega_0 = 1.82 \pm 0.09$	$\sigma_{xy} = 5.00$	$\rho = 0.152$
Runs (3)	$\omega_1/\omega_0 = 1.81 \pm 0.04$	$\sigma_{xy} = 2.83$	$\rho = 0.262$
	$\omega_2/\omega_0 = 2.85 \pm 0.10$	$\sigma_{xy} = -13.2$	$\rho = -0.514$
Runs (4)	$\omega_1/\omega_0 = 1.80 \pm 0.08$	$\sigma_{xy} = 7.00$	$\rho = 0.254$
	$\omega_2/\omega_0 = 2.88 \pm 0.11$	$\sigma_{xy} = 2.00$	$\rho = 0.064$

follows: If we have a variable r = (x,y) then the variance in r is related to those of x and y by:

$$\sigma_r^2 = \left[\frac{dr}{dx}\right]^2 \sigma_x^2 + \left[\frac{dr}{dy}\right]^2 \sigma_y^2 + 2\left[\frac{dr}{dx}\frac{dr}{dy}\right]\sigma_{xy} \qquad 8.4$$

where σ_{xy} is the "covariance" of x and y and is defined by:

$$\sigma_{xy} = \sum_{i=1}^{n} (\bar{x} - x_i)(\bar{y} - y_i) \qquad 8.5$$

Putting, as in our case, $x = \omega_1$ or ω_2 and $y = \omega_0$ makes $r = x/y$ and:

$$\frac{\sigma_r^2}{r^2} = \frac{\sigma_x^2}{x^2} + \frac{\sigma_y^2}{y^2} + \frac{2\sigma_{xy}}{xy} \qquad 8.6$$

The correlation coefficient $\rho = \sigma_{xy}/\sigma_x\sigma_y$ measures the degree to which x and y are correlated. If $\rho = 0$, no correlation exists and for $\rho = 1$, x and y can be said to completely correlated. σ_{xy} and ρ are given for the frequency ratios tabulated in Table 8.4, where the fairly low values of ρ indicate no large correlation between ω_1 and ω_0. The weighted means of the ratios ω_1/ω_0 and ω_2/ω_0 are shown in Table 8.5.

TABLE 8.5

THE WEIGHTED MEANS OF THE FREQUENCY RATIOS IN TABLE 8.4

$$\omega_1/\omega_0 = 1.81 \pm 0.03$$

$$\omega_2/\omega_0 = 2.86 \pm 0.07$$

8.4 THE ASYMMETRY PARAMETER η

Solutions of Equation 2.17 were calculated as described in Chapter 2 for values of η from 0.00 to 1.00 in steps of 0.05, and from these solutions the ratio ω_1/ω_0 was obtained for these values of η and plotted in Figure 2.3. In order to interpolate between these values and obtain η for the frequency ratios in Table 8.5 Newton's divided difference interpolation formula was used, and the following values of η extracted:

From ω_1/ω_0: $\eta = 0.289 \pm 0.029$

From ω_2/ω_0: $\eta = 0.25 \pm 0.07$

The weighted mean of these two values is:

$$\eta = 0.283 \pm 0.017$$

8.5 THE QUADRUPOLE INTERACTION FREQUENCY ω_Q

The solutions of Equation 2.17 also yield the ratio ω_0/ω_Q as a function of η as plotted in Figure 2.2 and for the above value of η we have

$$\omega_0/\omega_Q = 6.51 \pm 0.09$$

Using the weighted mean for ω_0 we obtain the following value for the quadrupole interaction frequency:

$$\omega_Q = 125.8 \pm 1.9 \quad \text{Mrad/sec}$$

8.6 THE ELECTRIC FIELD GRADIENT V_{zz}

Assuming that Ta^{181} is well described by the collective model, and that the intrinsic quadrupole moment Q_0 for the 482 KeV level equals that of the ground state, one can obtain the quadrupole moment Q for the 482 KeV level from the formula:

$$Q = Q_0 \frac{3K^2 - I(I+1)}{(I+1)(2I+3)} \qquad 8.7$$

Using the value of Q_0 obtained by McGowan et al[14] for the ground state by coulomb excitation and taking K = 5/2, I = 5/2:

$$Q(482 \text{ KeV}) = 2.53 \pm 0.10 \times 10^{-24} \text{ cm}^2$$

This value of Q and the above value for ω_Q yields, through equation 2.13, the following absolute value for the electric field gradient at Hf lattice sites in HfO_2:

$$V_{zz} = 13.1 \pm 0.6 \times 10^{17} \text{ volts/cm}^2$$

8.7 ZERO TIME POINT SHIFTS IN THE DATA

To investigate the shifts, if any, in the points in the time curves representing zero time that occurred as a function of time or angle, time curves were generated analytically by convolving the time response function for runs (3) and (4), as shown in Figure 7.3 with a FWHM of 1.3 nsec, with an exponential decay time curve with the form:

$$W(\theta,t) = (1+A_2P_2(\cos\theta)G_{22}(t))\exp(-\lambda t) \quad 8.8$$

Where the $G_{22}(t)$ attenuation function contained the theoretical amplitudes for a I = 5/2 level and η = 0.283 and the experimental oscillation frequencies from the uncorrected data. From these curves the position of the half-height point on the leading edge of the time curve was found relative to the time zero point for θ = 180 and 90 degrees and compared with the experimental time curves obtained from runs (3) and (4).

It was found that small shifts occurred in one of the two 90 degree positions used when compared to the other 90 degree position and the 180 degree position. These shifts amounted to about 0.5 nsec and are believed to be caused by changes in the prevailing magnetic fields with position, affecting the gain of the tube and hence the triggering level and triggering time. A full treatment of the time shifts of this sort has been made by Wagner et al[29]

Adjustments were made to the shifted data to align it with the remaining data, the frequency analysis was repeated to obtain the results in Table 8.1, and the two 90 and 180 degree runs from runs (4) totalized. Figure 8.5 shows the $G_{22}(t)$ function obtained from these totalized runs.

8.8 THE AMPLITUDES OF THE $G_{22}(t)$ FUNCTION

The Fourier power spectrum of the $G_{22}(t)$ function of Figure 8.5 is shown in Figure 8.6. The amplitudes s_{2n} from equation 2.14 of the three frequency components in that function are proportional to the square roots of the heights of the three identified peaks in the power spectrum. The solid curve through the experimental points is a sum of three cosines with frequencies corresponding to the centroids of the power spectrum peaks and the

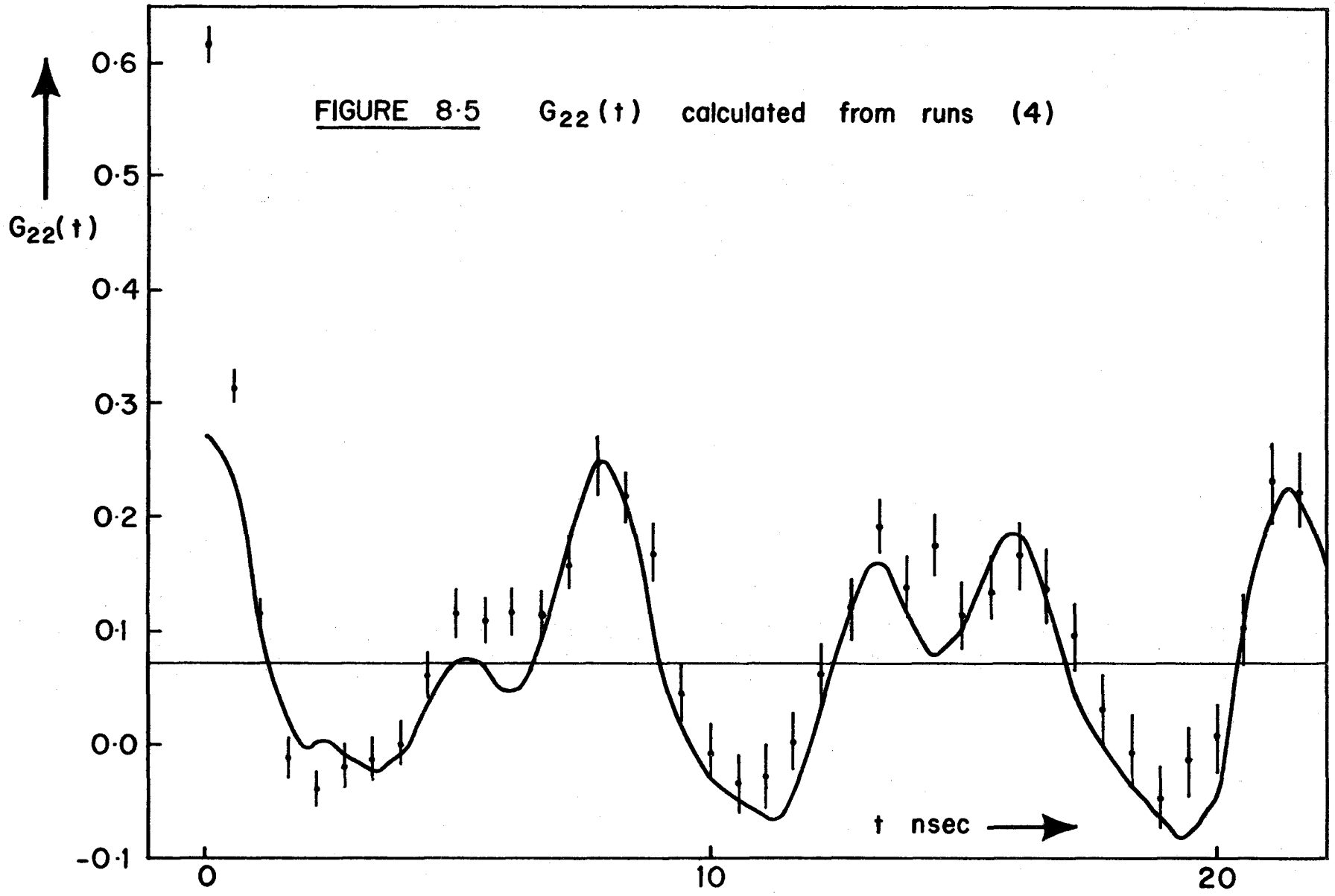
FIGURE 8·5 $G_{22}(t)$ calculated from runs (4)
$G_{22}(t)$
0·6
0·5
0·4
0·3
0·2
0·1
0·0
-0·1
0
10
20
t nsec

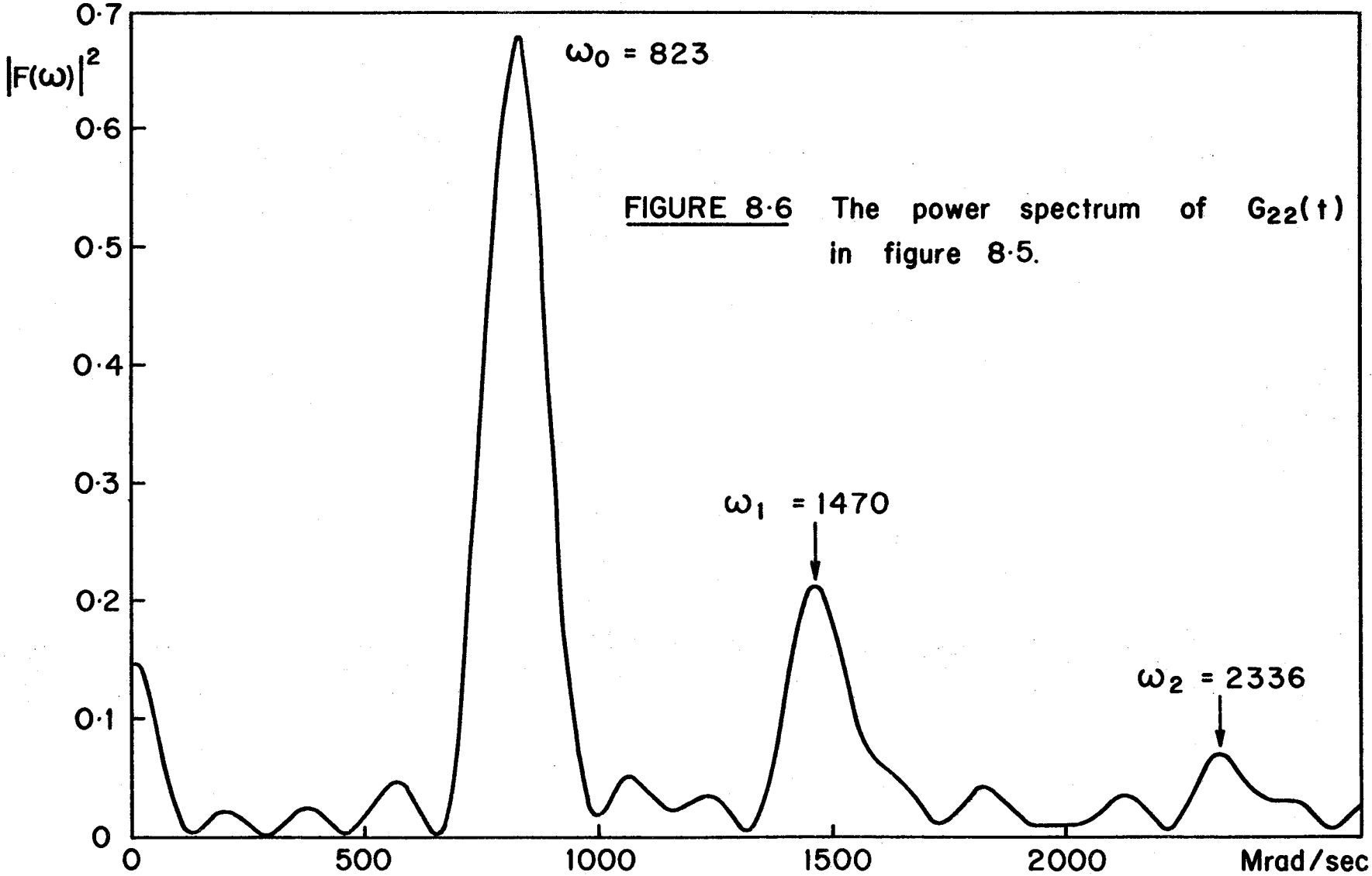

FIGURE 8·6 The power spectrum of $G_{22}(t)$ in figure 8·5.

amplitudes in the ratio of the square roots of the peak heights adjusted to obtain the best fit through the data with a suitable s_{20} "dc component". From this fit the following values values for the s_{2n}, uncorrected for time resolution and solid angle effects were obtained:

$$s_{20} = 0.070 \qquad s_{21} = 0.107$$
$$s_{22} = 0.060 \qquad s_{23} = 0.034$$

The dc component s_{20} corresponds to the hard core value of the attenuation, as described in Chapter 2, and is not affected by the finite time resolution, only by the solid angle effects discussed in Chapter 3. Thus a reasonable estimate of the solid angle effect can be obtained from the ratio of the experimental and theoretical hard core values. Reference (10) gives the theoretical hard core component for $\eta = 0.283$ and $I = 5/2$ as 0.216 so the solid angle diminishes the amplitudes in our case by the factor 0.216/0.070.

The correction for the diminuation of the amplitudes by the finite time resolution can be estimated from the form of Figure 4.2. Applying these two corrections gives the following values for the $G_{22}(t)$ amplitudes compared to the theory:

	EXPERIMENTAL	THEORETICAL
s_{20}:	0.22 ± 0.02	0.216
s_{21}:	0.38 ± 0.03	0.354
s_{22}	0.27 ± 0.04	0.284
s_{23}	0.24 ± 0.06	0.145

The error in the experimental values includes the standard deviation from the mean of the amplitudes as calculated from the individual power spectra of runs (4) and the experimental uncertainty in the measurement of the time resolution. Comparing the above values shows reasonable agreement except for s_{23}, but it should be born in mind that the Fourier analysis methods are much less sensitive to the amplitudes of the oscillations than the frequencies, because the latter are independant of the value of the time resolution. Also the amplitudes do not change rapidly with η. However, the above results indicate the measured value of η is a reasonable one.

8.9 THE FREQUENCY DISTRIBUTION WIDTH δ

It was hoped to extract a measurement of the frequency distribution width δ discussed in Chapter 2

from the widths of the power spectrum peaks after subtraction of the component due to the finite time interval represented by the data. However, this was not possible for two reasons; firstly, the widths add as their squares and the contribution from frequency distributions, being of the order of 5% of the centroid frequency, is almost completely masked by that of the time interval. This can be seen by comparing Figures 4.1 and 8.4.

Secondly, the exact width due to the time interval is, to some extent, uncertain through the influence of the statistical spread of the data which increases exponentially with time, degrading the contribution of the data to the power spectrum. In other words, the rectangular time interval function $\Pi(t)$ is modified by the effect of the statistics. Further studies are to be made of this and other effects on the power spectrum.

CHAPTER 9

THE CONCLUSIONS

The main features of the results obtained in this work and those of Marest et al[20] and Gerdau et al[21] for the quadrupole interactions of Ta^{181} in HfO_2 are set out for comparison in Table 9.1.

Marest et al was only able to extract the single fundamental frequency ω_o and the electric field gradient V_{zz}. Gerdau obtained four complete sets of results; (a) from Fourier analysis of data obtained from a source annealed for four hours at 1100 K, (b) from a least squares fit to the theoretical expression using the Fourier analysis results as a first approximation, (c) from Fourier analysis of data from the same source annealed for a further 48 hours at 1100 K and 8 hours at 1500 K, (d) from a least squares fit of that data. No data was presented from an unannealed source.

No significant changes in the measured frequencies were observed in the author's work before and after annealing for four hours at 1200 K but Gerdau noticed a small change when the further annealing was applied, although

TABLE 9.1

COMPARISON OF THE RESULTS OBTAINED BY THE AUTHOR WITH THOSE OF MAREST ET AL[20] AND GERDAU ET AL[21]

	ω_0	ω_1	ω_2	ω_Q	η	V_{zz} V/cm^2
	Mrad/sec					
AUTHOR	819 ± 10	1483 ± 25	2350 ± 50	125.8 ± 1.9	0.283 ± 0.027	13.1 ± 0.6
MAREST	780 ± 70	-	-	-	-	13.5 ± 1.2
GERDAU(a)	857 ± 8	1469 ± 19	2405 ± 110	125.5 ± 2.5	0.37 ± 0.03	-
GERDAU(b)	-	-	-	130.0 ± 1.3	0.33 ± 0.05	-
GERDAU(c)	843 ± 8	1435 ± 10	2323 ± 56	122.4 ± 2.5	0.38 ± 0.03	-
GERDAU(d)	-	-	-	126.9 ± 1.3		13.2 ± 0.6

their two values of ω_0 did not move outside the range of their respective experimental errors. This indicates that the annealing applied in this work and the initial annealing applied by Gerdau was ineffective and that more vigorous heat treatment is necessary before any re-ordering of the crystal structure can be observed.

The value of ω_0 obtained from this work agrees with that of Marest et al within their large experimental uncertainty but is slightly lower than that obtained by Gerdau et al in (a). Our value of ω_1 is in agreement with that of Gerdau for their partially annealed source but is higher than that for their more fully annealed source. All the values of ω_2 are consistent within the fairly large experimental errors and there is reasonable agreement between the values of ω_Q obtained by Gerdau and that obtained by us.

Some discrepancy exists between the values of η obtained by us and Gerdau; their values remain consistently higher than ours for both their source states. They were able to extract a measurement for their frequency distribution width from both the Fourier and least squares fit analyses but do not explain exactly how the former was achieved. The values of the electric field gradient V_{zz} are in excellent agreement.

In comparing the above results it is worth bearing in mind the differences in performance of the systems used by us and Gerdau and his co-workers. They used a three counter system to measure W(180,t) and W(90,t) simultaneously with NaI scintillators mounted on 56 AVP photomultiplier tubes. This gave them a considerable gain in count rate over our simpler system employing two detectors with one plastic and one NaI scintillator. They could use the improved statistics to widen the time interval in the Fourier analysis and to advantage in their least squares fit. However, their time resolution for the 133-482 KeV cascade was limited to 2.4 nsec FWHM which is close to the time period of their measured ω_2 whose amplitude must have been heavily degraded.

Our system used the experience gained over the past few years with fast photomultipliers for the measurement of short nuclear lifetimes in a deliberate attempt to achieve as good a time resolution as possible. A figure of 1.3 nsec FWHM was attained using the low noise RCA 8575 tubes and plastic on the 482 KeV gamma ray detector. This helped us considerably in the measurement of ω_2 and the effect of the better time resolution can be seen by comparing the structure detail that was resolved in our measured $G_{22}(t)$ function shown in Figure 8.5 with those of Gerdau et al in their paper.

Direct confirmation of the above results by the calculation of the electric field gradient V_{zz} from the known crystal structure has not been undertaken at present because of the complexity of the task, especially as the nature of the chemical bonds, that is, the degree of ionic and covalent mixing between the hafnium and oxygen atoms is, to some extent, uncertain. However, there is reasonable agreement between our results and those of Gerdau and co-workers and tne non-zero value of η is consistent with a non-cubic structure for HfO_2. The results also confirm the uniquness of η.

REFERENCES

1. K. Siegbahn, Beta and Gamma-Ray Spectroscopy, Chap. XIX (North Holland Publishing Co., Amsterdam) 1955

2. A. Abragam and R. V. Pound, Phys. Rev. 92 (1953) 943.

3. E. Heer and T. B. Novey, Solid State Physics, eds. F. Seitz and D. Turnbull (Academic Press Inc., New York)Vol. 9 1959.

4. R. M. Steffen and H. Frauenfelder, Perturbed Angular Correlations, Chap I, eds. E. Karlsson, E. Matthias and K. Siegbahm (North Holland Publishing Co., Amsterdam) 1964.

5. K. Alder, E. Matthias, B. Olsen, W. Schneider and R. M. Steffen, Chap. III of above, 247.

6. E. Matthias, W. Schneider and R. M. Steffen, Phys. Rev. 125 (1962) 261.

7. E. Matthias, W. Schneider and R. M. Steffen, Phys. Lett. 4 (1963) 41.

8. J. C. Raich and R. C. Good, Amer. J. Phys. 31 (1963) 356.

9. E. Matthias, W. Schneider and R. M. Steffen, Arkiv for Fysik, 24 (1963) 97.

10. R. Beraud, I. Berkes, J. Daniere, G. Marest and R. Rougny, Nucl. Instrum. Meth. 67 (1969) 41.

11. J. F. Boulter, W. V. Prestwich and B. Arad, Can. J. Phys., 47 (1969) 591.

12. R. M. Bracewell, The Fourier Transform and its Applications, (McGraw-Hill Book Co.) 1965.

13. C. M. Lederer, J. M. Hollander and I. Perlman, Table of Isotopes, (John Wiley & Sons Inc., New York) 6th. ed. 351.

14. F. F. McGowan and P. H. Stelson, Phys. Rev. 109 (1958) 901.

15. P. J. Ouseph and F. L. Canavan, Chap. III of Reference (4), 264.

16. P. J. Ouseph and F. L. Canavan, Phys. Lett. 3 (1962) 143.

17. R. W. Sommerfeldt and L. Schecter, Phys. Lett. 3 (1962) 5.

18. M. Salomon, L. Boström, T. Lindqvist and M. Perez, Phys. Lett. 5 (1962) 13.

19. M. Salomon, L. Boström, T. Lindqvist, M. Perez and M. Zwanziger, Arkiv För Fysik, 27 (1964) 20.

20. G. Marest, I. Berkes, G. Bougnot, and R. Beraud, Compt. Rend., 262B (1966) 367.

21. E. Gerdau, J. Wolf, H. Winkler and J. Braunsfurth, Proc. Roy. Soc., 311A (1969) 197.

22. L. Passerini, Gazz. Chim. Italiana, 60 (1930) 771.

23. S. Geller and E. Corenzwit, Analyt. Chem., 25 (1953) 1774.

24. J. Adam and M. D. Rogers, Acta. Cryst., 12 (1959) 951.

25. W. Baun, Science, 140 (1963) 1330.

26. R. F. Post and L. J. Schiff, Phys. Rev., 80 (1950) 1113.

27. E. Gatti and V. Svelto, Nucl. Instrum. Meth., 4 (1959) 189.

28. J. F. Boulter, W. V. Prestwich and T. J. Kennett, to be published in Nucl. Instrum. Meth.

29. H. F. Wagner and M. Forker, Nucl. Instrum. Meth. 69 (1969) 197.